2017

Flatland plasmonics and nanophotonics based on graphene and beyond

Pai-Yen Chen
Wayne State University, pychen@wayne.edu

Christos Argyropoulos
University of Nebraska-Lincoln, christos.argyropoulos@unl.edu

Mohamed Farhat
Hamad Bin Khalifa University

J. Sebastian Gomez-Diaz
University of California, Davis

Review article

Open Access

Pai-Yen Chen*, Christos Argyropoulos, Mohamed Farhat and J. Sebastian Gomez-Diaz

Flatland plasmonics and nanophotonics based on graphene and beyond

Abstract: In this paper, we review and discuss how the recently discovered two-dimensional (2D) Dirac materials, particularly graphene, may be utilized as new efficient platforms for excitations of propagating and localized surface plasmon polaritons (SPPs) in the terahertz (THz) and mid-infrared (MIR) regions. The surface plasmon modes supported by the metallic 2D materials exhibit tunable plasmon resonances that are essential, yet missing, ingredients needed for THz and MIR photonic and optoelectronic devices. We describe how the atomically thin graphene monolayer and metamaterial structures based on it may tailor and control the spectral, spatial, and temporal properties of electromagnetic radiation. In the same frequency range, the newly unveiled nonlocal, nonlinear, and nonequilibrium electrodynamics in graphene show a variety of nonlinear and amplifying electromagnetic responses, whose potential applications are yet unexplored. With these 2D material platforms, virtually all plasmonic, optoelectronic, and nonlinear functions found in near-infrared (NIR) and visible devices can be analogously transferred to the long-wavelength regime, even with enhanced tunability and new functionalities. The spectral range from THz to MIR is particularly compelling because of the many spectral fingerprints of key chemical, gas, and biological agents, as well as a myriad of remote sensing, imaging, communication, and security applications.

*Corresponding author: Pai-Yen Chen, Department of Electrical and Computer Engineering, Wayne State University, Detroit, MI 48202, USA, e-mail: pychen@wayne.edu
Christos Argyropoulos: Department of Electrical and Computer Engineering, University of Nebraska-Lincoln, Lincoln, NE, 68588, USA
Mohamed Farhat: Qatar Energy and Environment Research Institute (QEERI), Hamad Bin Khalifa University, Qatar Foundation, Doha, Qatar
J. Sebastian Gomez-Diaz: Department of Electrical and Computer Engineering at the University of California, Davis, One Shields Avenue, Kemper Hall 2039, Davis, CA 95616, USA

1 Introduction

Graphene is a single layer of sp^2-bonded carbon atoms arranged in a hexagonal structure, which can be seen as a two-dimensional (2D) version of the three-dimensional (3D) crystalline graphite. Ever since it was discovered in 2004 [1], graphene has attracted wide attention due to its exotic electronic, thermal, mechanical, and optical properties. Graphene has been reported to have an ultra-high carrier mobility, exceeding 200,000 cm^2/Vs and Fermi velocity (v_F) of 10^8 cm/s at low temperatures, strong quantum Hall effect, unexpectedly high opacity (i.e. an optical transmittance of 97.7% for a graphene monolayer), and mechanical flexibility with a Young's modulus of 0.5 TPa [1–6]. The energy-momentum dispersion relation of graphene is linear over a wide range of energies. As a result, electrons in graphene behave as massless Dirac fermions with an energy-independent velocity, and a high-quality graphene monolayer can therefore exhibit the exceptional ballistic transport distance exceeding several tens of μm [7]. In addition, graphene's unique band structure and finite density of states result in the pronounced ambipolar electric field effect [1–6], for which the charge carriers can be tuned continuously between electrons and holes in concentrations as high as 10^{14} cm^{-2} via chemical doping or electrostatic gating [8]. Recently, chemical vapor deposition (CVD) has become a mature technique to fabricate large-area mono-, bi-, or few-layer graphene at low temperatures [9–11]. Graphene is considered to be one of the most promising material candidates for post-silicon nanoelectronic devices and interconnects, as well as transparent electrodes for optoelectronic devices, such as solar cells and flat-panel displays [2].

In a different context, graphene, known as the first ever 2D material, uniquely possesses a gapless Dirac-cone-like band structure, making it an ideal material platform for interacting with light from microwave to ultraviolet [2]. The discovery of graphene's inherent plasmonic-like

properties has further enriched this multifunctional nano-material platform [12–28]. Historically, localization and guiding of electromagnetic energy below the diffraction limit have been of great interest. One and perhaps the only viable path toward this goal at near-infrared (NIR) and visible frequencies are excitations of surface plasmon polaritons (SPPs) in noble metals, forming surface charge density waves propagating along the metal-dielectric interface, leveraging the dispersive and negative permittivity of metals, within a growing field of research called "plasmonics" [29–32]. More interestingly, compared with conventional metal-based plasmonics, graphene plasmonics covers a relatively less explored wavelength range from terahertz (THz) to mid-infrared (MIR) [25–28, 33]. It is known that practical applications of plasmonics still present significant challenges, mostly because traditional metals are notoriously plagued by losses. Recent advances in the fabrication of high-quality graphene monolayers may realize ultrahigh carrier mobilities, which presents exciting possibilities for the progress in low-loss plasmonics [25–27]. The large-area, low-defect, highly crystalline graphene is expected to raise the surface plasmon lifetime along its surface ideally up to hundreds of optical cycles,

thus circumventing a major challenge of noble-metal plasmonics [19, 22]. Besides, the extreme light-matter interaction in the atomically thin graphene is followed by a significant wavelength shortening and dramatically enhanced local fields [12–28]. The surface plasmon bounded to one-atom-thick graphene sheet shows numerous favorable properties, which make graphene a promising alternative to typical plasmonic materials. More interestingly, a high-quality graphene may support not only the propagating and localized plasmons with potentially higher plasmon lifetimes, but also dynamically tunable electromagnetic responses and optical transitions that can be controlled by chemical/photo/electrostatic doping and magnetic means [34–39], thanks to the finite density of states of 2D conductors that allow a tunable plasma frequency. Recent experimental works have demonstrated that graphene may support tightly bounded surface waves in the infrared spectrum, with gate-tuned and strong field localization [27, 28], as shown in Figure 1. This intriguing property has been envisioned to realize flatland transformation optics and metamaterials [19].

Graphene plasmonics has become the subject of intensive research, with extremely promising applications
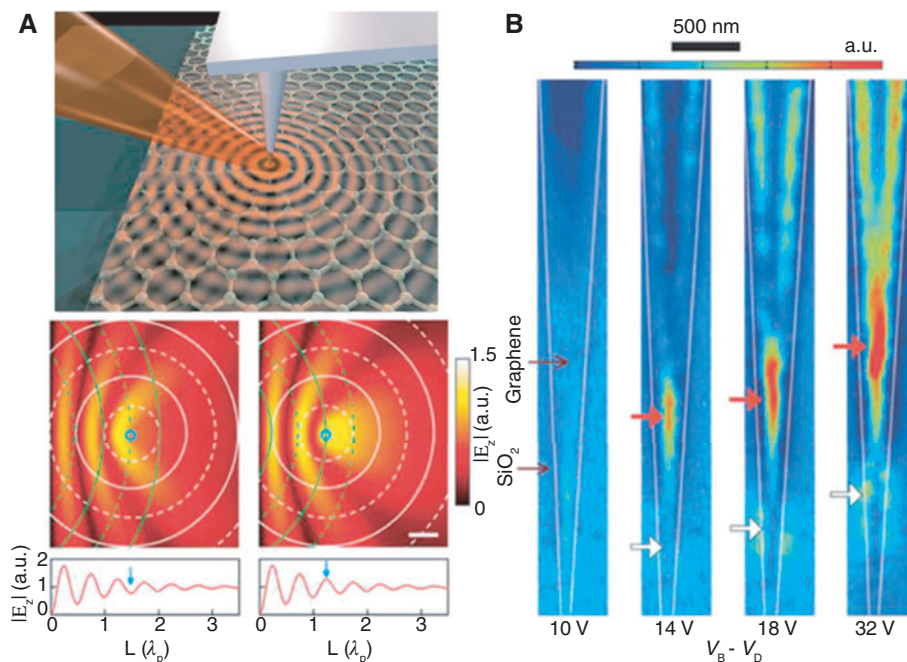
Figure 1: Schematic of SPPs in graphene [27, 28].
(A) Top panel: schematics of the experiment on how to launch and detect SPPs on graphene based on near-field scanning optical microscopy, in which an infrared laser illuminates a metallic tip to locally excite SPPs, and the near-field SPP signal is scattered by the tip into the far-field in order to be detected. Bottom panel: snapshots of destructive (left) and constructive (right) interference of SPP waves underneath the tip (blue circles); the profiles of electric field amplitude underneath the tip versus its distance to the left edge, where the arrow indicates the half wavelength of SPPs. (B) Near-field amplitude images of graphene plasmons tuned by an electrostatic backgate. Red and white arrows denote the positions of resonant local SPP modes on a tapered graphene ribbon.

for various gate-controlled optoelectronic devices [12–28], including metamaterials [22, 24, 34, 39], switches [40], filters [41, 42], polarizers [21], invisibility cloaks [20], hyperbolic metasurfaces [43–46], nanoantennas and radiation apertures [47–52], phase shifters [53, 54], nonreciprocal components [55], modulators [56–58], photodetectors [42], photomixers [59, 60], and oscillators [17], spanning frequencies from THz to MIR. In general, for those applications, the ultrafast, low-power, and broadband modulations of light's amplitude, phase, or both, are potentially possible. In this work, we will briefly review the recent developments on theory and experiment, as well as practical applications of graphene plasmonics that offer an exciting flatland platform for strong light-matter interactions in the THz and infrared spectra.

This review paper is organized as follows: in Section 2, we discuss and review scenarios in which graphene has been used to excite strong and tunable plasmonic responses at the nanoscale. First, we review some recently observed SPPs supported by graphene monolayers and nanostructures (e.g. metamaterials) due to the imaginary component of graphene's Drude (intraband) conductivity. With the dynamic conductivity derived from the semiclassical model, the Maxwell's equations can be solved exactly for an arbitrary electric current induced on the graphene surface. We then discuss how graphene plasmonics may be controlled to enhance propagation, radiation, scattering, and extinction of long-wavelength infrared and THz waves. In Section 3, we discuss the nonlinear and nonequilibrium optical responses in graphene and their potential applications in plasmon amplification and tunable THz lasing, as well as diverse nonlinear optical phenomena. Finally, we briefly review the other newly discovered 2D Dirac materials and their plasmonic and nanophotonic applications in Section 5.

2 Enhanced plasmonic properties in graphene monolayer and nanostructure

An atomically thin graphene monolayer can be considered as a transverse conducting sheet with a complex-valued surface conductivity $\sigma(\omega) = \sigma' + j\sigma''$ that can be well modeled by first-principle calculations [61, 62], random phase approximations [17, 22, 63], or semiclassical models [12, 13]; here, we assume an $e^{j\omega t}$ time dependence throughout this work. In the long-wavelength region, the surface conductivity of graphene monolayer depends on its Fermi energy E_F (or chemical potential),

which can be largely tuned either by chemical doping [35, 38], external static electric field [64] (leading to an isotropic scalar surface conductivity), or external static magnetic field via Hall effect [15, 65] (leading to a gyrotropic and tensor surface conductivity). In the absence of static magnetic field, the semiclassical conductivity of graphene, which includes both intraband conductivity σ_{intra} and interband conductivity σ_{inter}, is given by

$$\sigma(\omega, \mu_c, \Gamma, T) = \sigma_{\text{intra}} + \sigma_{\text{inter}}$$
$$= -\frac{jq^2(\omega - j\tau^{-1})}{\pi\hbar^2}\left[\int_{-\infty}^{+\infty}\frac{|\varepsilon|}{(\omega - j\tau^{-1})^2}\frac{\partial F(\varepsilon)}{\partial\varepsilon}d\varepsilon\right.$$
$$\left. - \int_0^{+\infty}\frac{F(-\varepsilon) - F(\varepsilon)}{(\omega - j\tau^{-1})^2 - 4(\varepsilon/\hbar)^2}d\varepsilon\right], \qquad (1)$$

where $F = 1/(1 + \exp[(\varepsilon - E_F)/(K_B T)])$ is the Fermi-Dirac distribution, ε is the energy, T is the temperature, q is the electron charge, $\hbar$ is the reduced Planck's constant, K_B is the Boltzmann's constant, and τ is the impurity-limited relaxation time associated with plasmon loss in graphene. The first and second terms in Eq. (1) account for the intraband and interband contributions, respectively. In the long-wavelength region, σ_{intra} dominates over σ_{inter}. Therefore, for a doped graphene with $|E_F| \gg k_B T$ and for photon energy far below the interband transition threshold, $\hbar\omega < 2|E_F|$, Eq. (1) can be conveniently expressed using Drude-type dispersion:

$$E_x = \left[\sigma_{\text{graphene}}\frac{p}{p-d} - i\frac{\eta_{\text{eff}}}{2}\alpha_{\text{ABC}}\left(1 + \frac{1}{k_{\text{eff}}^2}\frac{\partial^2}{\partial x^2}\right)\right]\left(H_y^- - H_y^+\right) = Z_s^{\text{TM}}J_x$$
$$E_y = \left[\sigma_{\text{graphene}}\frac{p}{p-d} - i\frac{\eta_{\text{eff}}}{2}\alpha_{\text{ABC}}\right]\left(H_x^- - H_x^+\right) = Z_s^{\text{TE}}J_y \qquad (2)$$

where the Drude weight $D = q^2 E_F/\hbar^2$. The intrinsic relaxation time can be expressed as $\tau = \mu E_F/qV_F^2$ where v_F is the Fermi velocity and μ is the measured dc mobility. For instance, with a mobility of 10,000 cm²/V s, a conservative value $\tau \approx 10^{-13}$ s is measured for $E_F = 0.1$ eV. In general, the interband conductivity is on the order of $q^2/\hbar$. For $\hbar\omega$, $|E_F| \gg K_B T$, σ_{inter} can be approximately expressed as [15, 16]

$$\sigma_{\text{inter}} \approx \frac{q^2}{4\hbar}\left(\theta(\hbar - 2E_F) - j\frac{1}{\pi}\ln\left[\frac{2|E_F| - \hbar(\omega - j\tau^{-1})}{2|E_F| + \hbar(\omega - j\tau^{-1})}\right]\right), \qquad (3)$$

where $\theta(\cdot)$ is the step function. In the NIR and visible spectral ranges, where the photon energy $\hbar\omega \gg E_F$, $K_B T$, the interband contribution dominates and the optical conductivity is constant, given by

$$\sigma = \frac{q^2}{4\hbar}\tanh\left(\frac{\hbar\omega - 2\varepsilon_F}{4K_B T}\right) \approx \frac{q^2}{4\hbar}. \qquad (4)$$

As a result, graphene is almost transparent (~97.7% transmittance) over a wide range of wavelengths from NIR to visible and cannot sustain surface plasmons.

Typically, the Fermi energy of graphene can be tuned over a wide range by an externally applied bias (electrostatic gating), as the Fermi energy in graphene is related to the carrier concentration n_s by [6]

$$n_s = \frac{2}{\pi(\hbar v_F)^2} \int_0^\infty \varepsilon[F(\varepsilon - E_F) - F(\varepsilon + E_F)]d\varepsilon. \tag{5}$$

From Eqs. (2) and (5), we note that the Drude weight of graphene $D \propto E_F \propto \sqrt{n_s}$ can be tuned by varying the carrier density of graphene. By placing a p^+/n^+-doped polysilicon or metal gate behind the insulating oxide that supports the graphene monolayer, the carrier concentration in graphene and, therefore, its dynamic conductivity can be tuned over a wide range by applying different gate voltages. Due to the electron-hole symmetry in the electronic band structure of graphene, both negative and positive signs of Fermi energy provide the same value of complex conductivity. For an N-layer graphene, one may assume $\sigma_{N\text{-layer}} = N\sigma$, which is approximately valid for at least up to $N = 10$, as validated by the experimental data [33, 58].

The unique features of ballistic transport and ultra-high electron mobility in a high-quality graphene may provide a relatively large value of $|\text{Im}[\sigma]/\text{Re}[\sigma]|$ [19]. This implies that a graphene monolayer can be seen as a reactive sheet (impedance surface) with low loss in the THz-to-MIR region, effectively playing a role analogous to a frequency selective surface (FSS) without the need for lithographically patterning graphene [20]. Figure 2 reports the complex-valued conductivity of graphene with different Fermi energies. It is seen that the imaginary part of graphene's conductivity (or surface impedance $Z_s = 1/\sigma$) is tunable with respect to the Fermi energy. Such fascinating behavior appears naturally suited to manipulate the electromagnetic scattering and near-field enhancement for THz and long-wavelength infrared waves.

In the THz and infrared regions, a uniform or patterned graphene (e.g. metasurface) has been demonstrated to achieve the scattering reduction or enhancement for its covered dielectric/conducting objects, which has the iconic term of *graphene cloak* [20]. The physical principle behind the graphene cloak resides in the scattering cancellation effect, which was first validated in microwave experiments by using the copper FSS [66, 67]. For the graphene cloak in Figure 3A, the effective surface current yielded by the plasmon oscillations in graphene can be tailored to radiate "antiphase" scattered fields [66, 67]. Consequently, around the operating wavelength, a cancellation between the scattering fields contributed by the covered object and graphene may restore the incident wavefronts in the near- and far-field. This effect is, in general, independent of the polarization and incidence angle of the impinging wave and the position of the observer, since the surface impedance of graphene is isotropic without an external static magnetic field. Moreover, the tunable surface reactance of graphene related to $\text{Im}[\sigma]$ may enable a frequency-reconfigurable cloaking device. In addition to camouflaging and mirage applications, the graphene cloak has been proposed to improve the performance of near-field sensors and photodetectors in the interference/scattering-rich environment [68, 69]. We note that most subdiffractive measurements are usually performed in the very-near-field of the details to be imaged, and therefore, their accuracy is intrinsically limited by the disturbance introduced by the close proximity of the sensing instrument, e.g. a sensing probe that may perturb the near field distributions and influence the measurement [68]. A graphene cloak may greatly suppress the
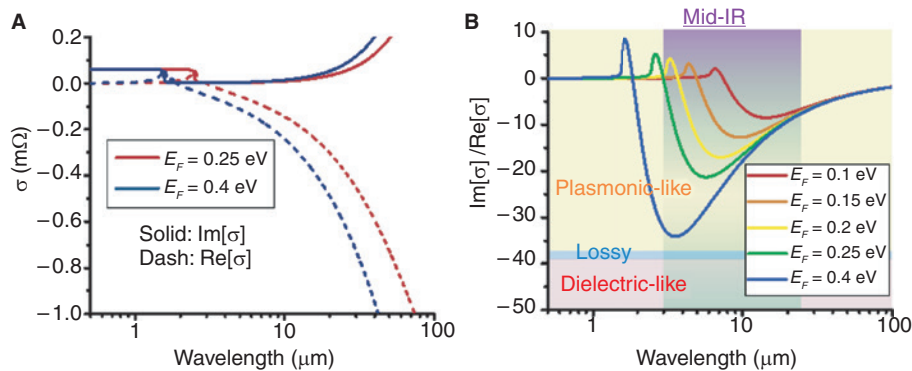
Figure 2: Wavelength dependence of the (left) real and imaginary parts and (right) their ratio of dynamic conductivity for a graphene monolayer, whose dual plasmonic or dielectric properties can be tuned by the Fermi energy of graphene.
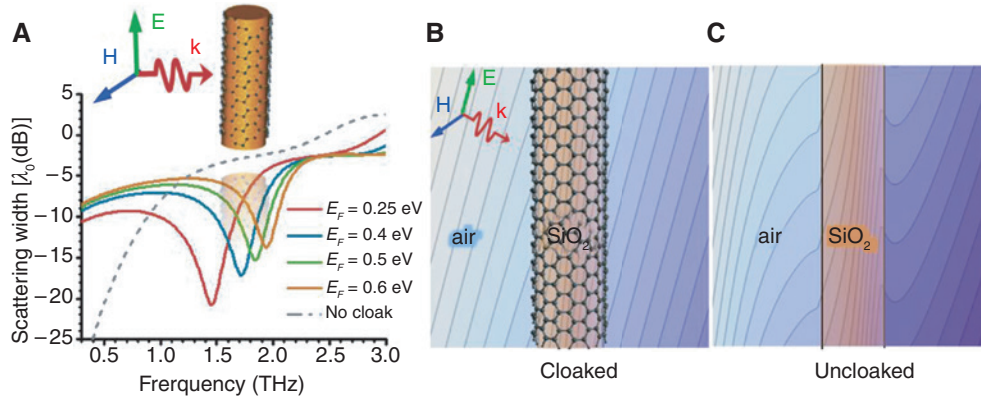
Figure 3: (A) Normalized total SW of a SiO$_2$ cylinder with diameter $2a = 40$ μm and permittivity $\varepsilon_d = 3.9\,\varepsilon_0$, without and with graphene cloak (i.e. graphene-wrapped microtube). Here, the Fermi energy of graphene is varied to show its great tunability on the design frequency. The phases of magnetic fields on the E plane (B) with and (C) without the graphene cloak with Fermi energy $E_F = 0.25$ eV are shown at the operating frequency $f_0 = 1.45$ THz.

undesired multipath scattering and noise for the highly sensitive sensor and probe.

Figure 3A considers, as an example, a dielectric cylinder covered by a graphene-microtube cloak [70], whose scattering response can be calculated using the Lorentz-Mie scattering theory with the impedance boundary condition. The induced averaged surface current on the graphene sheet is proportional to the discontinuity of tangential magnetic fields: $\mathbf{H}_{tan}\big|_{r=a^+} - \mathbf{H}_{tan}\big|_{r=a^-} = \sigma(\hat{\mathbf{r}} \times \mathbf{E}_{tan}\big|_{r=a})$, where a is the radius of the dielectric cylinder. For an isotropic surface with negligible cross-polarization coupling, such as a graphene monolayer, the total scattering width (SW), as a quantitative measure of the overall visibility of the object at the frequency of interest, can be computed as the sum of Mie scattering coefficients. In the quasi-static limit, the closed-form cloaking condition for a dielectric cylinder under the TM-polarized illumination can be derived as $X_{diel} = 2/[\omega a(\varepsilon_d - \varepsilon_0)]$, where ε_d and ε_0 are permittivities of dielectric cylinder and background medium, respectively. Obviously, an inductive surface, such as the doped graphene monolayer, is required for efficiently suppressing the scattering from a moderate-size dielectric object, under the illumination of THz waves. Figure 3A also presents the total SW for an infinite SiO$_2$ cylinder with permittivity $\varepsilon_d = 3.9\,\varepsilon_0$ and diameter $2a = 40$ μm, covered by a graphene-wrapped microtube with different Fermi energies; here, an uncloaked SiO$_2$ cylinder is also presented for comparison (gray dash line). From Figure 3A, we see how significant scattering reduction can be achieved by using an ultrathin and conformal graphene cloak. The cloaking frequency may be widely tuned by varying the Fermi energy of graphene, thus realizing a tunable and switchable cloaking device. Around the operating frequency, it

may be possible to tailor the total SW by over two orders of magnitude, simply through the variation of Fermi energy. Figure 3B and C show, respectively, the near-field phase contours of the magnetic field on the E plane for a cloaked ($E_F = 0.25$ eV) and uncloaked SiO$_2$ cylinder at the operating frequency $f_0 = 1.5$ THz. In both cases, the plane wave excites the geometry from the left side and contours are plotted on the same color scale. It is found that for all positions around the cylinder, significant scattering reduction and restoration of original phase fronts can be obtained when compared with an uncloaked dielectric cylinder. It is also worth mentioning that the electromagnetic radiation can enter the graphene cloak, thus enabling an "invisible" sensor for applications in the low-noise, cross-talk-free THz sensing, imaging, communication, and spectroscopy systems, as well as wireless networks, such as inter/intra-chip ultrafast links, indoor systems, and internet-of-nanothings highlighted in Refs. [71–73].

On the other hand, for a conducting cylinder with moderate cross-section covered by a thin spacer, the following cloaking condition is obtained, generalizing the results of Ref. [69]: $X_{cond} \cong -\omega\mu_0 a[(\gamma^2 - 1)/(\gamma(\gamma^2 + 1))]$, where γ is the radius ratio between the graphene cloak and the conducting cylinder and μ_0 is the permeability of background medium. As observed from this formula, an ultrathin cloak with capacitive surface reactance is required to effectively reduce the scattering from a conducting cylinder. A nanostructured graphene monolayer, such as a graphene-nanopatch metasurface [69], can have a surface reactance tuned from inductive to capacitive, as a function of the graphene's kinetic inductance and the geometric patch capacitance. This dual-reactive property may allow for cloaking both dielectric and conducting objects.

The graphene cloak may also be exploited to conceal a 3D dielectric/conducting object, such as a dielectric spherical particle [74, 75] or a more complicated geometry like 3D finite wedges [76]. Moreover, the multiband operation and cloaking of larger objects may also be conceivable by using multiple graphene layers, which offer more degrees-of-freedom and allow suppressing a larger number of scattering orders. A theoretical discussion on the possibility of cloaking a dielectric sphere with multiband operation can be found in Ref. [74].

The research on tailoring light scattering properties using graphene has initiated a substantial number of studies dedicated to graphene nanostructures, such as ribbons [22, 24] and disks [64, 77, 78], of which finite size effects and boundary conditions are important, yielding new electromagnetic phenomena and opening up the way of dynamically modulating the amplitude, phase, and polarization states of THz and infrared radiation over an ultrathin impedance surface. The tunable electromagnetic response is one of the most exciting areas in current plasmonic and metamaterial research [79, 80], since it may add a large degree of control and flexibility to the exotic electromagnetic properties. Here, we note two main features of the graphene-based metamaterial and metasurface: (1) the large kinetic inductance yielded by subwavelength confinement of surface plasmons in the structured graphene may help scaling the size of metamaterial inclusions to deeply subwavelength, thus enhancing the homogeneity and granularity of artificial materials, and (2) the field-effect-tuned surface impedance can be achieved, as the dynamic conductivity of graphene is controlled by its carrier concentration.

Figure 4A presents a metasurface formed by a collection of specific graphene surface inclusions (e.g. a lithographically patterned graphene). Each graphene surface inclusion, when illuminated by external radiation, may generate a localized or mixed-type semilocalized SPPs, leading to the strong resonant scattering. The scattering fields ($\mathbf{E}_s$, $\mathbf{H}_s$) are responsible for the localized, field-dependent surface current $\mathbf{k}_s \sim \sigma \mathbf{E}_0^{tan}$ inside each graphene inclusion. The polarizability α and the equivalent electric dipole moment per unit length $\mathbf{p}$ (parallel to the surface) are given by $\mathbf{p} = (-j/\omega) \int_{S_{in}} \mathbf{k}_s ds = \alpha \mathbf{E}_0^{tan}$, where σ and S_{in} are the conductivity and the enclosed area, respectively, of each graphene inclusion [81]. In the metasurface configuration (Figure 4A), the induced dipole moment of an inclusion, considering the interdipole interactions via the dyadic Green function $\mathbf{G}$ [82], can be expressed as
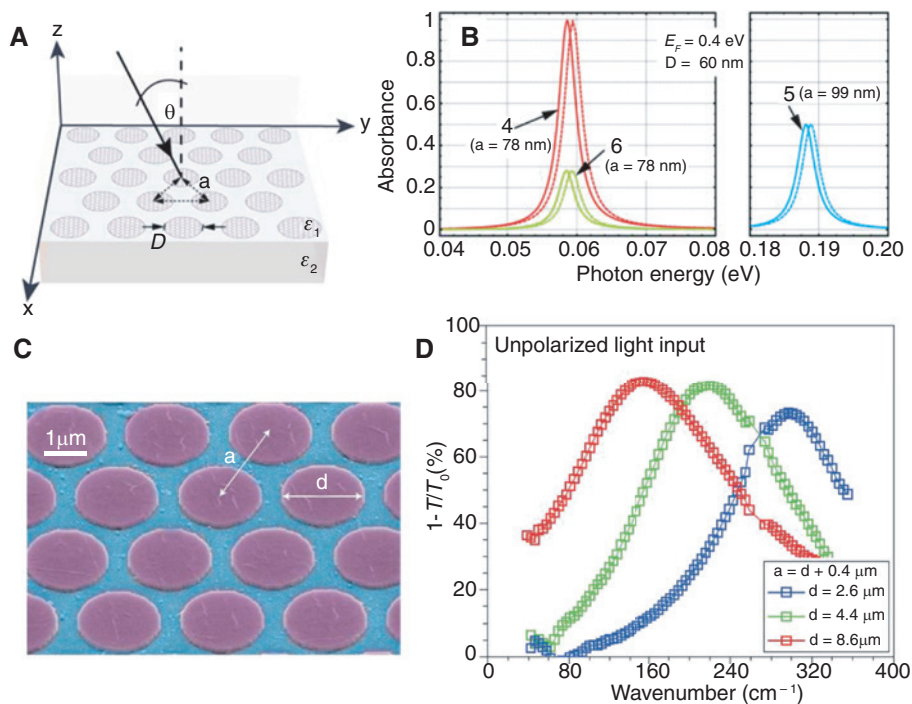
Figure 4: (A) Schematics of a planar array of doped graphene nanodisks of diameter $D = 60$ nm and Fermi energy $E_F = 0.4$ eV and (B) the corresponding absorption for (left) an asymmetric interface with $\varepsilon_1 \neq \varepsilon_2$ and (right) a symmetric interface with $\varepsilon_1 = \varepsilon_2$; the lower-index medium has relative permittivity $\varepsilon_1 = 1$. (C) Scanning electron microscopy image for nanofabricated infrared metamaterials made of multilayer circular graphene patches. (D) Measured electromagnetic wave rejection ratio of the graphene metamaterials in the MIR and far-infrared spectrum [41].

$$\mathbf{p} = p_0 \hat{x} = \frac{\mathbf{E}_0^{\text{tan}}}{\alpha^{-1} - \sum_{(N_x, N_y) \neq (0,0)} \mathbf{G}(\mathbf{r}_{N_x N_y}) \cdot \hat{\boldsymbol{x}} \cdot \hat{\boldsymbol{x}}}. \tag{6}$$

The equivalent surface impedance of the metasurface, defined as the ratio of local electric field to surface current density $\mathbf{J}_s = J_s \hat{x} = j\omega \mathbf{p}/(d_x d_y)$ is given by $Z_s = E_0/J_s - \eta_0/2$, where η_0 is the free space impedance and d_x, d_y are the lattice spacing of metasurface. Figure 4B shows the spectral absorption of a graphene metasurface depicted in Figure 4A, considering the dipole-dipole mutual coupling between adjacent graphene inclusions. It is seen that despite its ultrathin profile, the graphene metasurface provides a perfect infrared absorption. Further, the peak frequency may be wideband tunable via the electrostatic gating, thus being of interest for a variety of optical applications, such as tunable filters and absorbers. We also note that in a symmetric environment (e.g. a graphene immersed in the uniform medium), a maximum absorption of 50% can be achieved, which is consistent with what is predicted from the optical theorem [24]. The perfect absorption can be achieved by considering the asymmetric environment (e.g. a dissimilar dielectric interface with $\varepsilon_1 \neq \varepsilon_2$ or a patterned graphene on top of a metallic ground plane [77, 78, 83, 84]).

Recent progress in the growth and lithographic patterning of large-area epitaxial graphene presents great opportunities for the practice of graphene-based THz and infrared metamaterials. Figure 4C shows a graphene-nanopatch metamaterial recently invented by IBM Corporation [41]. Hence, wafer-scale, large-area graphene metamaterials have been successfully fabricated and characterized. To realize frequency selective optical properties, the plasmonic resonances are introduced in a graphene-insulator stack by lithographically patterning it into microdisks arranged in a triangular lattice. Figure 4D shows the measured rejection ratio (extinction in transmission) spectrum for the graphene metamaterial in Figure 4C with different dimensions; here, the transmission extinction is defined as $1 - T/T_0$, where T and T_0 are the transmission through the quartz substrate with and without the graphene-insulator stack, respectively. A measured peak transmission of $\sim 80\%$ is achieved with a stacked device made of five graphene layers. It is evident that by changing the dimensions of the fabricated graphene patch and lattice constant, the resonant peak can be adjusted in the MIR spectrum. When the number of graphene layers is increased, the peak intensity increases significantly and the resonance frequency upshifts [41].

Another geometry of interest in our investigation is based on lithographic graphene nanoribbon (GNR) arrays

shown in Figure 5A [64], where conduction currents are confined within the *disjoint* GNRs with strong reactive coupling between neighboring plasmonic inclusions that have subwavelength width d and period p. We note that according to the semiempirical results [6], the bandgap of a GNR with width $p - d > 500$ nm is not open yet. Thus, the previously derived surface conductivity for a graphene monolayer is still valid. One can analytically solve the problem using the averaged boundary condition, for which a discontinuity on the tangential magnetic field on the metasurface is related to the averaged surface current by the equivalent surface impedance Z_s [82]:

$$\mathbf{E}_x^- = -i\frac{\eta_{\text{eff}}}{2}\alpha_{ABC}\left[\sigma_g \frac{p}{p-d} + \left(1 + \frac{1}{k_{\text{eff}}^2}\frac{\partial^2}{\partial x^2}\right)\right](\mathbf{H}_y^- - \mathbf{H}_y^+) = Z_s^{\text{TM}}\mathbf{J}_x$$

$$\mathbf{E}_y^- = -i\frac{\eta_{\text{eff}}}{2}\alpha_{ABC}(\mathbf{H}_x^- - \mathbf{H}_x^+) = Z_s^{\text{TE}}\mathbf{J}_y, \tag{7}$$

where α_{ABC} is called grid parameter and ε_{eff}, $\eta_{\text{eff}} = \sqrt{\mu_0/\varepsilon_{\text{eff}}\varepsilon_0}$, and $k_{\text{eff}} = \omega\sqrt{\mu_0\varepsilon_{\text{eff}}\varepsilon_0}$ are the relative permittivity, wave impedance, and wave number of the effective host medium [82], respectively. The superscripts TE and TM in Eq. (7) represent the transverse-magnetic and transverse-electric incident waves, respectively. The surface reactance of metasurface $\text{Im}[Z_s]$ may be tuned from inductive to capacitive, as a function of the tunable kinetic inductance of GNRs and the geometric capacitance [66]. It has been shown in Ref. [66] that the effective surface inductance/capacitance can be derived from Eq. (7), and the intriguing dual-reactive property on a single metasurface may provide many new possibilities for tailoring the THz and MIR scattering properties [66]. The dual-reactive property of graphene metasurface also introduces an extra pole and zero in the Lorentzian dispersion of surface impedance, which may enable the enhanced, multiband, or broadband extinction and scattering [78], as well as the possibility of cloaking both dielectric and conducting objects using the same graphene metasurface (but varying E_F) [66].

Figure 5A considers a GNR array separated from the metallic ground plane by a thin dielectric layer. Such structure exhibits interesting electromagnetic properties, which are equivalent to a grounded magnetic-metamaterial slab (e.g. arrays of split-ring resonators) with effective permeability being negative [78, 84–86]. The grounded dielectric slab with a subwavelength thickness offers a magnetic inductance [87] as a function of the height of dielectric slab, which may resonate with the geometric capacitance and the kinetic inductance of the GNR array. Therefore, the frequency dispersion of this
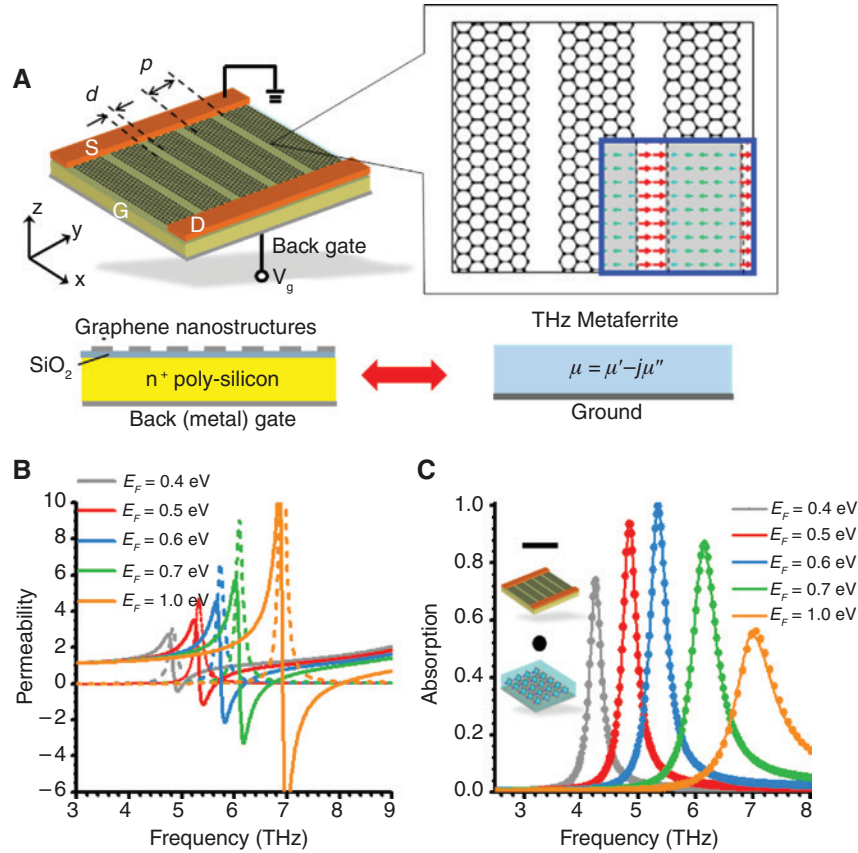
Figure 5: (A) Schematics of THz metaferrite composed of a planar array of GNRs on top of a SiO_2/p$^+$-poly-Si slab backed by a metallic back-gate, which can be equivalent to a ferrite with relative permeability $\mu = \mu' - j\mu''$ backed by a conducting plane, as shown in the bottom panel. (B) Frequency dispersion of effective permeability for a graphene metaferrite with different biased Fermi energy (solid line: real, dash line: imaginary). (C) Absorption spectra for the graphene metaferrite of (A). The thickness of $=SiO_2$/p$^+$-poly-Si is 25 nm/2 µm, and the dimensions of nano-patch are period $d = 1$ µm and gap $d/p = 0.25$.

graphene metamaterial can be tailored by varying either the period/gap and carrier density of GNRs (which tunes the geometric capacitance and kinetic inductance), as well as the dielectric constant and thickness of the dielectric slab (which tunes the substrate-induced inductance). In addition, the metallic and dielectric layers may enable the electrostatic back-gating, leading to a tunable THz and infrared metamaterial. Figure 5B shows the frequency dependency of effective permeability retrieved for the graphene magnetic metamaterial (or metaferrite) in Figure 5A under normal incidence. The solid and dashed lines represent the real and imaginary parts of effective permeability, respectively. The geometry of GNRs are $g = 0.5$ µm and $a = 4$ µm, and the dielectric slab is made of SiO_2 with thickness $t = 1$ µm. From Figure 5B, it is seen that the Lorenzian resonance in the effective permeability can be tuned from low or negative to positive. A low reflection corresponding to a high absorption can be accomplished, provided that the equivalent permeability $\mu = \mu' - j\mu''$ is tailored to the optimum value for a ground-back

magnetic-film absorber: $\mu' \approx 0$ and $\mu'' \approx 1/k_0 t$ [78], where k_0 and t are the free space wave number and the thickness of graphene metaferrite, respectively. Figure 5C presents the absorption spectra for the graphene metaferrites in Figure 5B, showing large and tunable absorption with respect to the doped Fermi energy of graphene. The GNR-based metamaterial may be of interest for a variety of long-wavelength infrared applications, including the artificial magnetic conductor, ultracompact Salisbury absorbing films [88], polarization filters [84], and selective thermal emitters or absorbers [89]. Recent experimental works have demonstrated that the THz extinction of a planar GNR array can be tailored by varying its geometry or by electrostatically gating GNRs [41].

In addition to their scattering properties, nanostructured graphene also exhibits fascinating properties from the in-plane point of view. Specifically, it is able to implement ultrathin metasurfaces able to support different topologies, from isotropic to hyperbolic, and going through the σ-near-zero (canalization) regime [43, 44, 46,
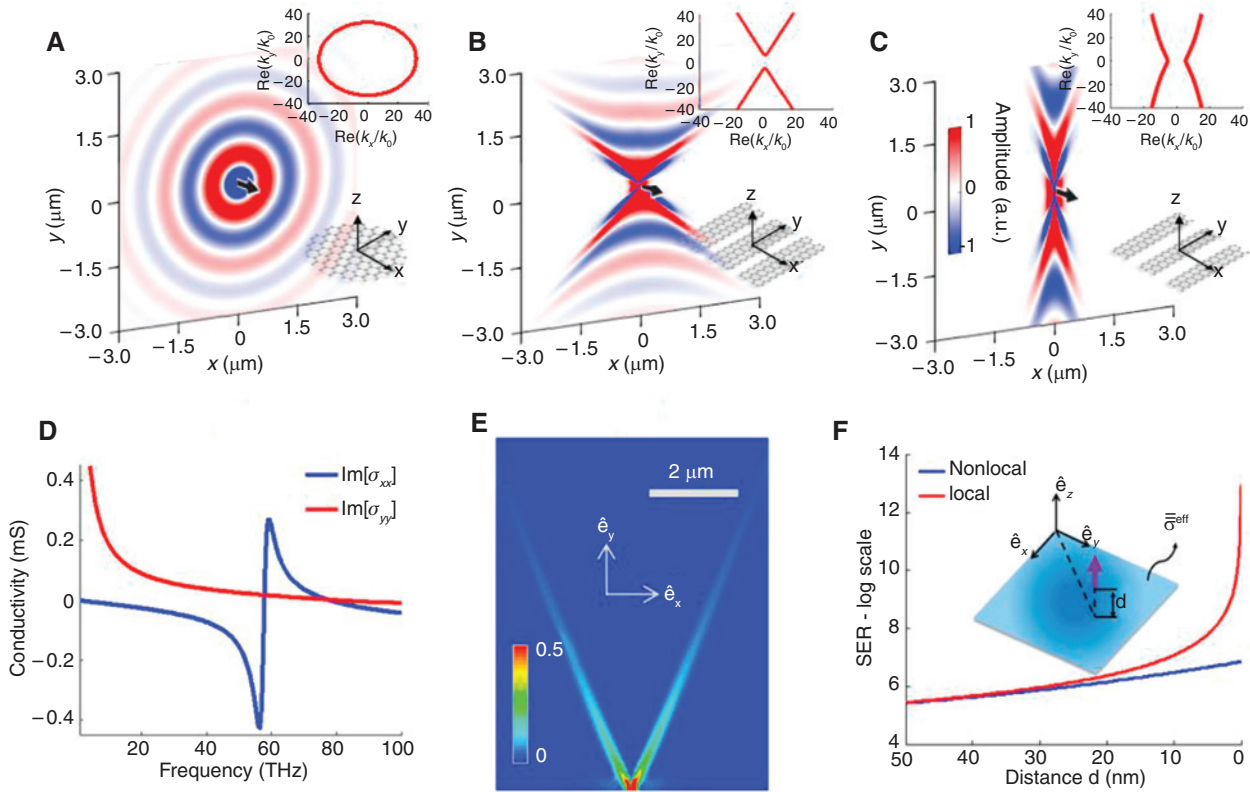
Figure 6: Hyperbolic, isotropic, and σ-near zero metasurfaces implemented by nanostructured graphene.
(A)–(C) Color maps illustrate the z-component of the electric field excited by a z-directed emitter (black arrow) located 10 nm above the metasurface [44]. Insets present the isofrequency contour of each metasurface (top) and a possible graphene-based implementation (bottom). (A) Isotropic metasurface. (B) Hyperbolic metasurface. (C) σ-near zero metasurface. (D) Example of the in-plane effective conductivity tensor realized by a densely packed array of graphene strips, implementing several types of topologies at different frequencies [43]. (E) Full-wave verification of hyperbolic plasmons excited over nanostructured graphene [44]. (F) Dramatic enhancement of the spontaneous emission rate (in log scale) of a dipole versus its distance over a hyperbolic metasurface [45]. Results are computed considering (nonlocal) and not (local) considering graphene's inherent spatial dispersion.

90] (see Figure 6). Hyperbolic metasurfaces have recently been introduced using graphene nanostructures – i.e. ultrathin 2D materials – at THz and far-infrared (FIR) frequencies [43] and patterned silver surfaces at optics [91], and they provide very exciting properties, such a relatively simple fabrication using standard techniques, resilience to volumetric losses, compatibility with integrated circuits, and an easy external access to the propagating surface wave using near-field techniques. Importantly, hyperbolic metasurfaces support the propagation of low-loss and extremely confined surface plasmons able to strongly interact with the surrounding media. In addition, these structures provide large degrees of freedom to manipulate the supported plasmons, enabling advanced functionalities, such as canalization, negative refraction, dramatic enhancement of light-matter interactions, or the routing of plasmons toward specific directions within the layer. Let us assume an infinitesimally thin

homogeneous anisotropic metasurface described by conductivity tensor $\bar{\bar{\sigma}} = \mathrm{diag}(\sigma_{xx}, \sigma_{yy})$, where the different components may be in general complex, and the structure has been assumed to be passive, free of magneto-optical and nonlocal effects, and aligned along our reference system. By investigating the sign of $\mathrm{Im}[\sigma_{xx}]$ and $\mathrm{Im}[\sigma_{yy}]$, the metasurface topology can easily identified and engineered. For example, Figure 6A shows an *isotropic elliptic topology* ($\mathrm{Im}[\sigma_{xx}] < 0$, $\mathrm{Im}[\sigma_{yy}] < 0$), where the excited transverse magnetic SPPs propagate with similar characteristics across the entire layer. A natural example of isotropic metasurface is graphene, an inductive 2D material where $\mathrm{Im}[\sigma_{xx}] = \mathrm{Im}[\sigma_{yy}] < 0$. We should note that unbalancing the conductivity components, but keeping their inductive (metallic) nature, leads to designs able to favor the propagation of SPPs toward one direction over others [43]. Figure 6B shows a metasurface that implements a *hyperbolic topology*, which arises when the structure behaves as

a metal (inductive, $\text{Im}[\sigma] < 0$) along one direction and as a dielectric (capacitive, $\text{Im}[\sigma] > 0$) along the orthogonal one, i.e. $\text{sgn}(\text{Im}[\sigma_{xx}]) \neq \text{sgn}(\text{Im}[\sigma_{yy}])$. The last topology considered here is the *σ-near-zero regime* (see Figure 6C), which appears at the metasurface topological transition [43] and canalizes the propagating energy towards a specific direction. It is important to mention that, even though ideal hyperbolic metasurfaces are expected to provide infinite wave confinement and local density of states, their response is limited in practice by the presence of losses, nonlocality arising due to the periodicity (in case of patterned configurations) and the intrinsic spatial dispersion of the composing materials [45]. An array of densely packed graphene strips [43] (see inset of Figure 6A–C) is an ideal platform to implement any metasurface topology at THz and far infrared frequencies, with the important advantage to provide inherent reconfiguration capability to the resulting structure. The in-plane effective conductivity tensor of such metasurface can be homogenized as $\sigma_{xx}^{\text{eff}} = L\sigma\sigma_C / (W\sigma_C + G\sigma)$, $\sigma_{yy}^{\text{eff}} = \sigma(W/L)$, $\sigma_{xy}^{\text{eff}} = \sigma_{yx}^{\text{eff}} = 0$, where $\sigma_C = j\omega\varepsilon_0\varepsilon_{\text{eff}}(L/\pi)\ln[\csc(\pi G/2L)]$ describes the near-field coupling between adjacent strips [69], W and G are the strips width and separation, and L is the unit-cell period. We should stress that the homogeneous condition $L \ll \lambda_{\text{SPP}}$ must be satisfied for such equations to be valid, where λ_{SPP} is the plasmon wavelength. An example of this homogeneous model, which takes into account that wave propagation is inductive (capacitive) along (across) the strips, is illustrated in Figure 6D. This figure shows that the proposed structure can indeed implement different topologies versus frequency. Rigorous full-wave simulations shown in Figure 6E confirm the ability of the nanostructured graphene to support hyperbolic plasmons, while dramatically enhancing the spontaneous emission rate of emitters located nearby (Figure 6F). The graphene-based reconfigurable hyperbolic metasurfaces may pave the way toward the development of miniaturized devices able to extremely confine and dynamically guide light over ultrathin surfaces, with direct applications in communications, lensing, and sensors.

As previously pointed out, graphene has been experimentally demonstrated to support the surface wave at the THz and long-wavelength infrared wavelengths, with moderate loss and strong field localization. The extremely confined surface waves sustained by a graphene sheet may be of interest for passively guiding and actively gate-tuning/modulating THz and infrared surface waves. The dynamically tunable dispersion relation and SPP wavelength of propagating surface waves may be expected to realize flatland SPP waveguides and transformation optics [19, 92]. The dispersion relation of SPP modes in graphene can be

computed by matching the *two-sided impedance boundary*, which, for TM surface waves illustrated in Figure 7A, can be expressed as

$$\frac{\varepsilon_2}{\varepsilon_1}\sqrt{\beta^2 - k_1^2} + \sqrt{\beta^2 - k_2^2} + \frac{\sigma}{j\omega\varepsilon_1}\sqrt{\beta^2 - k_1^2}\sqrt{\beta^2 - k_2^2} = 0, \qquad (8)$$

whereas for TE, the dispersion equation is

$$\frac{\mu_2}{\mu_1}\sqrt{\beta^2 - k_1^2} + \sqrt{\beta^2 - k_2^2} + j\omega\mu_2\sigma = 0, \qquad (9)$$

where β is the complex phase constant of surface wave and k_i, ε_i, and μ_i are the wave number, permittivity, and permeability of the ith medium, respectively. The type of surface waves supported on the monolayer depends on both signs and value of imaginary part of graphene's conductivity. In general, only modes on the proper Riemann sheet may provide meaningful physical wave phenomena, whereas leaky modes on the improper sheet can be used to approximate parts of the spectrum and to explain certain radiation phenomena [13–15]. Considering a freestanding graphene in vacuum ($\varepsilon_1 = \varepsilon_2 = \varepsilon_0$ and $\mu_1 = \mu_2 = \mu_0$), the eigenmodal solutions for Eq. (8) can be explicitly expressed as [13]

$$\beta = \sqrt{k_0^2 - \left(\frac{2\omega\varepsilon_0}{\sigma^2}\right)^2}, \qquad (10)$$

whereas the similar explicit solution for Eq. (9) is

$$\beta = \sqrt{k_0^2 - \left(\frac{\omega\mu_0\sigma}{2}\right)^2}. \qquad (11)$$

From Eqs. (10) and (11), we notice that if $\text{Re}[\sigma]$ is small and $\text{Im}[\sigma] < 0$ a TM-mode slow surface-wave exists at THz, FIR, and MIR wavelengths. In this case, the strongly confined TM mode arises from the plasmonic property of graphene with negative $\text{Im}[\sigma]$, (see Figure 2). However, if $\text{Im}[\sigma]$ is positive, a leaky mode on the improper Riemann sheet is obtained for the TM-mode surface wave. On the other hand, at wavelengths where $\text{Im}[\sigma] > 0$, the TE-mode surface wave can exist in the MIR region (see Figure 2). Unlike strongly localized TM-mode surface waves, TE-mode surface waves are only weakly localized at the surface. Besides, the plasmon losses and optical phonon scattering in the infrared spectrum may limit the propagation length of TE-mode surface waves.

Figure 7A shows (left panel) the schematic of a propagating SPP on graphene/insulator interface and (right panel) contours of real and imaginary phase
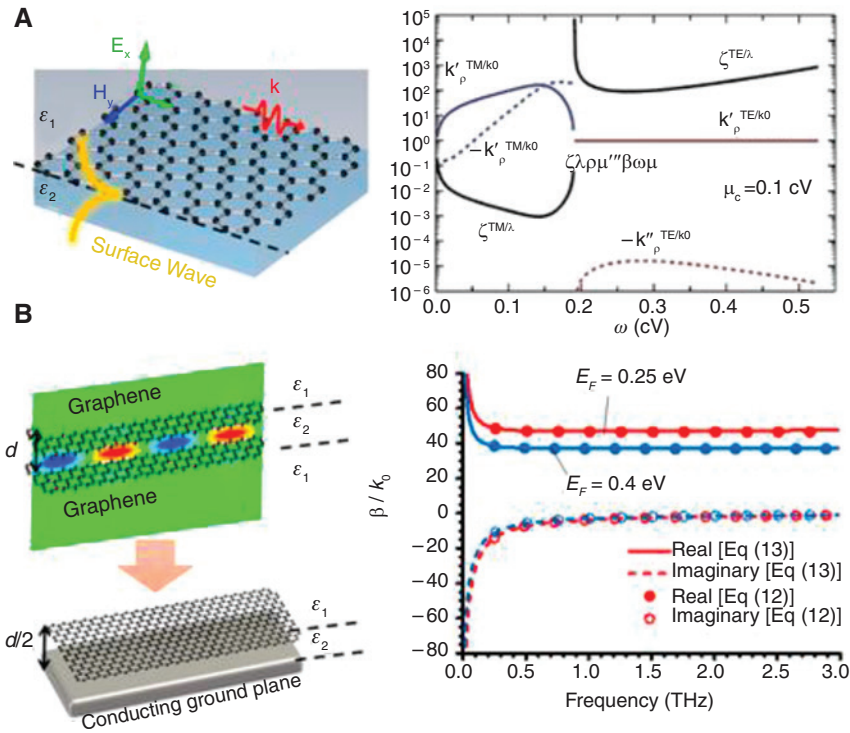
Figure 7: (A) Schematics of a propagating SPP (surface) wave on graphene (left) and the eigenmode dispersion: surface-wave wavenumber k and attenuation length ζ for a graphene monolayer with Fermi energy of 0.1 eV at room temperature for both TE and TM surface waves (right) [13]. (B) Schematics of a GPPWG and a simplified compact design inspired by the field symmetry of quasi-TEM mode (left). The complex phase constant of a GPPWG with thickness $d/2 = 50$ nm, supporting a quasi-TEM mode, is shown at the right side. Lines and symbols represent the eigenmodal solutions calculated by Eqs. (12) and (13), respectively.

constant (normalized by the free space wave number) for TM surface waves, varying the operating frequency and the Fermi energy of graphene. At very low photon energy, the TM surface wave is relatively fast ($\beta \cong k_0$) and poorly confined to the graphene surface. In the THz to MIR region, the surface wave is strongly confined and becomes slow ($\beta \cong k_0$), as energy is concentrated in the near field of graphene surface. We note that around the interband transition threshold ($\hbar\omega = 2|E_F|$), a moderate change in Fermi energy can dramatically change the sign of imaginary conductivity from negative to positive, thereby supporting TE surface waves. In the range of $\Gamma \ll \omega < 2|E_F|/\hbar$, only a strongly confined TM surface wave propagates. This TM mode is of particular interest since it is dispersive with the Fermi energy in the frequency range of interest. This allows one to tune and modulate the dispersion of surface waves. In contrast, the TE mode is poorly confined to the graphene sheet and it is essentially nondispersive. Since the TE and TM modes do not coexist, this allows one to make a wideband-tunable graphene polarizer, supporting the TE surface wave propagation for frequencies above the interband transition threshold [13–15].

Vakil and Engheta have theoretically shown that by designing inhomogeneous and nonuniform conductivity patterns across a graphene sheet [19] (e.g. using electrostatic gating), the flatland transformation optics devices can be realized. In Ref. [19], several numerical examples have been presented to demonstrate the infrared modulation and transformation functions. In Ref. [92], a flatland Fourier optics lens has been numerically studied for transforming a broadcasting surface wave from the source into perfect planar wavefronts on a graphene monolayer. So far, several groups have experimentally demonstrated the gate-tuning of SPP waves on a graphene ribbon by using the scatter-type scanning near-field microscopy. These measurements were based on the feedback scheme taken from atomic force microscopy, where the nanomanipulated nanotip is positioned and scanned in the immediate vicinity of graphene surface. The strong local field confinement and gate-tuning standing-wave field patterns due to the interference in a finite-length graphene ribbon have been successfully characterized in Refs. [27] and [28]. We believe that the advancement of nanotechnology and nanofabrication will benefit the rapidly expanding field of graphene plasmonic devices.

Traditionally, a subwavelength parallel-plate plasmonic waveguide, such as the metal-insulator-metal (MIM) heterostructure, can provide better control and confinement of the guided SPP modes [14]. Figure 7B (upper panel) shows a graphene parallel-plate waveguide (GPPWG), constructed with two parallel graphene sheets with widths much larger than the separation distance d (with the propagation axis oriented along the z-axis). In many senses, the propagation properties of this GPPWG are analogous to those of a MIM plasmonic waveguide, but suitable in the sub-THz to MIR wavelengths. For TM_z waves with magnetic field $H_x(y)$ exp$[j(\omega_t - \beta_z)]$, the complex eigenmodal phase constant β can be evaluated by solving the dispersion equation [14, 53]:

$$\tanh[\sqrt{\beta^2 - \omega^2\mu_0\varepsilon_2}\,h/2]\frac{\sqrt{\beta^2 - \omega^2\mu_0\varepsilon_2}}{\sqrt{\beta^2 - \omega^2\mu_0\varepsilon_1}}$$
$$= -\frac{\varepsilon_2}{\varepsilon_1 - j\sqrt{\beta^2 - \omega^2\mu_0\varepsilon_1}\frac{\sigma}{\omega}}, \tag{12}$$

where ε_2 and ε_1 are the material permittivity inside and outside the waveguide, respectively. When the separation between the graphene monolayers is reduced to a deep-subwavelength scale $h \ll \lambda_0$, the graphene waveguide supports a quasi-transverse electric-magnetic (TEM) mode [14, 53]. Under the long-wavelength approximation $h \ll \min(2\pi/|\omega\sqrt{\varepsilon_2\mu_0}|, 2\pi/|\omega\sqrt{\varepsilon_1\mu_0}|)$ and $\sigma\sqrt{\beta^2 - \omega^2\mu_0\varepsilon_2}/\omega\varepsilon_2, \sigma\sqrt{\beta^2 - \omega^2\mu_0\varepsilon_1}/\omega\varepsilon_1 \gg 1$, a simple explicit dispersion relation can be obtained as [14]

$$\beta/k_0 \cong \sqrt{\frac{\varepsilon_2}{\varepsilon_0}\left(1 - j\frac{2}{\mu_0\omega\sigma h}\right)}. \tag{13}$$

As expected, for sufficiently large conductivity, the permittivity of the outer cladding layer has a negligible effect on the complex phase constant β, since the mode is tightly confined between two graphene layers. For the quasi-TEM mode that, in principle, has no cutoff frequency, the longitudinal field E_z is nonzero but very small compared to the uniform transverse field E_x, provided that the waveguide dimension (h) is very small. Due to the symmetry of fields for the quasi-TEM mode, the GPPWG can be replaced by a half-size waveguide in Figure 7B (bottom panel), where a single graphene sheet is separated from a conducting ground plane by a half-thickness dielectric layer. Figure 7B (right side) presents the normalized phase constant β/k_1 for the graphene waveguide shown in Figure 7B (left side), filled with a 50-nm-thick SiO_2 ($\varepsilon_2 = 4\varepsilon_0$ and $d/2 = 50$ nm) in a background of air ($\varepsilon_1 = \varepsilon_0$). It can be seen that in the low-THz region, the quasi-TEM mode is relatively nondispersive, supporting a slow-wave propagation with strongly confined THz waves inside the waveguide, and a guided wavelength much smaller than the free-space wavelength $\lambda_g \ll \lambda_0$, thanks to the large kinetic inductance of graphene. For frequencies above sub-THz, the attenuation constant becomes small and the group velocity is almost constant without dispersion. In this case, a low-loss transmission line with moderate signal attenuation and dispersion is obtained [6]. From Figure 7B, it is seen that the phase constant of graphene waveguides is tunable by shifting the Fermi level of graphene, enabling reconfigurable transmission lines at sub-THz and THz frequencies. It is worth mentioning that at RF and microwave frequencies, some recent experiments have shown that graphene-based transmission lines may make a compact attenuator or terminator [93].

The transmission line model and transfer matrix method can be used to evaluate characteristics of THz/infrared components constituted by single/integrated graphene waveguides. The characteristic impedance of the graphene waveguide shown in Figure 7B can be defined as $Z_c = -E_y/H_x = \beta/\omega\varepsilon_2$, By combining the graphene waveguide in Figure 7B with a double gate (or the hybrid graphene/metal [back gate] waveguide configuration), the THz conductivity of graphene can be controlled by the applied gate voltage, thereby adjusting dynamically the propagation constant, phase velocity, and local impedance of a transmission line segment. It can be intuitively understood that the phase constant and characteristic impedance of a graphene transmission line can be tuned from relatively high (e.g. a pristine graphene with a small E_F) to low (e.g. a biased graphene with a large E_F). This is arguably the most significant advantage of graphene over conventional noble-metal plasmonic waveguides, providing an exciting venue to realize electronically programmable THz transmission lines, similar to their microwave counterparts realized by microstrip-lines loaded with varactors, diodes, or transistors.

Figure 8A illustrates an integrally gated transmission line based on the quasi-TEM GPPWG, backed by a metal gate. As an example to illustrate the potential of such reconfigurable THz transmission line, the device in Figure 8A can be used as a loaded-line phase shifter designed for THz phased arrays or THz modulators, with relatively low insertion loss, low return loss, and small phase error. In practical designs, the return loss is inherently present due to the reflection at the mismatched loaded-line. The design in the inset of Figure 8B consists of a 3-bit phase shifter with eight phase shift states: 0°/45°/90°/135°/225°/270°/315° [53, 94]. When gate voltages are applied, the length of each loaded section must be a multiple of half guided wavelength such that the
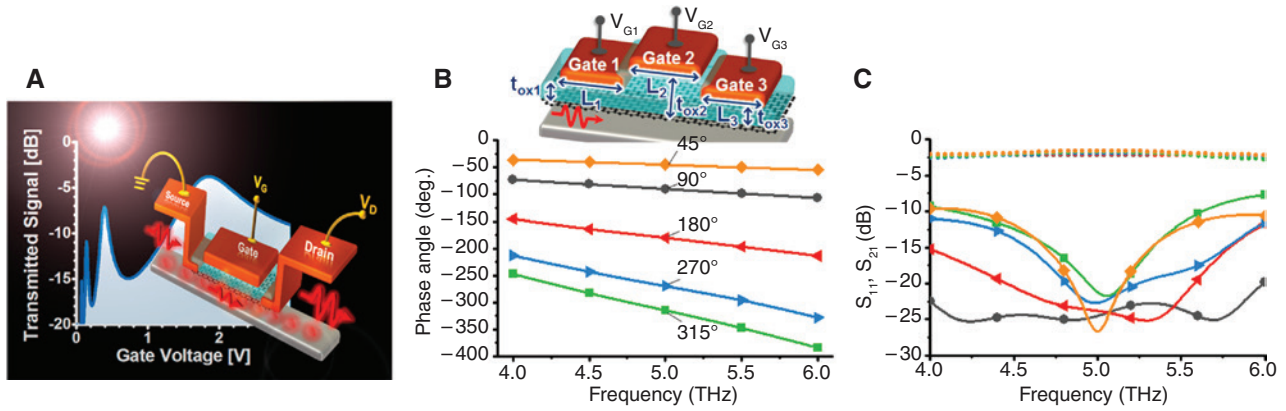
Figure 8: (A) Schematics of a hybrid electronic-plasmonic (plasmoelectronic) nanodevice, comprising a graphene field-effect-transistor (GFET) and a graphene plasmonic waveguide (GPWG). (B) Integrally gated graphene transmission line with digitized, spatially varying phase velocity and characteristic impedance. Such device may realize, for example, a 3-bit graphene-based phase shifter using three integrated gates. The simulated phase shift versus frequency shows accurate angles at the design frequency (5 THz). (C) Transmission (dashed) and reflection (solid) for the device in (B), showing moderate insertion and return losses.

impedance mismatch and return loss can be minimized. In order to create impedance matching for all binary states, the ith transmission line segment must satisfy the conditions $\beta_{\text{bias}} l_i = \pi/2$ and $\beta_{\text{unbias}} l_i - \beta_{\text{bias}} l_i = \Delta\phi_i$, where l_i and $\Delta\phi_i$ are defined as the gate length and relative phase shift between the unbiased and biased conditions for the ith section, respectively. The total phase shift is therefore obtained as $\Delta\phi = \Delta\phi_1 + \Delta\phi_2 + \Delta\phi_3$. In order to satisfy these conditions, the required Fermi energy and length for each bits need to be properly designed. For instance, if we want to produce phase shifts of 45° (bit 0), 90° (bit 1) and 180° (bit 2), the propagation constants must satisfy the relationships $\beta_1 = 4/5\,\beta_0$, $\beta_2 = 2/3\,\beta_0$ and $\beta_3 = 1/2\,\beta_0$, and the associated length of each line must satisfy the condition $\beta_{\text{bias}} l_i = \pi/2$. Figure 8B and C show numerical results for the magnitude of S_{21} and phase shifts of 45°, 90°, 180°, and 315°, respectively. These phase angles are obtained by applying the proper voltages to gate G1, G2, G3, and all, respectively. It is seen that good input return loss is obtained, with desired relative phase shifts at the design frequency $f_0 = 1.5$ THz. This graphene phase shifter may be applied to sub-THz, THz, and infrared high-gain, steerable phased-array antennas. The gated graphene waveguides, with tunable and strongly confined mode, may enable a number of chip-scale THz nanocircuit components, including switching, matching, coupling, power dividing or combining, and filtering devices [94].

In this context, it is important to emphasize that the response of graphene-based components, such as the aforementioned phase shifters or in-plane low-pass filters [95], can be strongly influenced by the intrinsic nonlocality (or spatial dispersion) of graphene [15, 54, 96–98]. This phenomenon arises due to the finite Fermi velocity of electrons in graphene, which are unable to follow the expected fast variations of the supported plasmons. In order to model this phenomenon, advanced wavenumber-dependent $\sigma(k_\rho)$ conductivity models of graphene have been derived [18, 96, 99]. Figure 9 illustrates the influence of spatial dispersion on phase shifters and a seventh-order low phase filters [54] implemented using the double gated graphene waveguides described above, and studies their responses as a function of the surrounding media. In this analysis, we first model graphene using the local description and then using a more accurate graphene model that takes nonlocal effects into account [96]. The results reveal that the intrinsic nonlocality of graphene upshifts the operation frequency of plasmonic components, limiting their reconfiguration capabilities, and degrading their overall response. More importantly, it is also found that the influence of spatial dispersion increases with the permittivity of the surrounding media, which is associated to the higher confinement of the supported plasmons in such cases. The study in [97] clearly confirms that graphene nonlocality must be rigorously taken into account in the development of plasmonic THz in-plane components.

The integration of several active graphene-based THz nanocircuit components, including a graphene THz antenna [47–49, 100, 101], into a single entity will present a fundamental step towards design architectures and protocols for innovative THz communications, biomedicine, sensing, and actuation [70–72]. In addition, a plasmonically resonant graphene patch is expected to realize a frequency-reconfigurable, electrically small THz antenna with moderate radiation efficiency and directionality [47–49, 100, 101]. It can be implemented either in planar or in
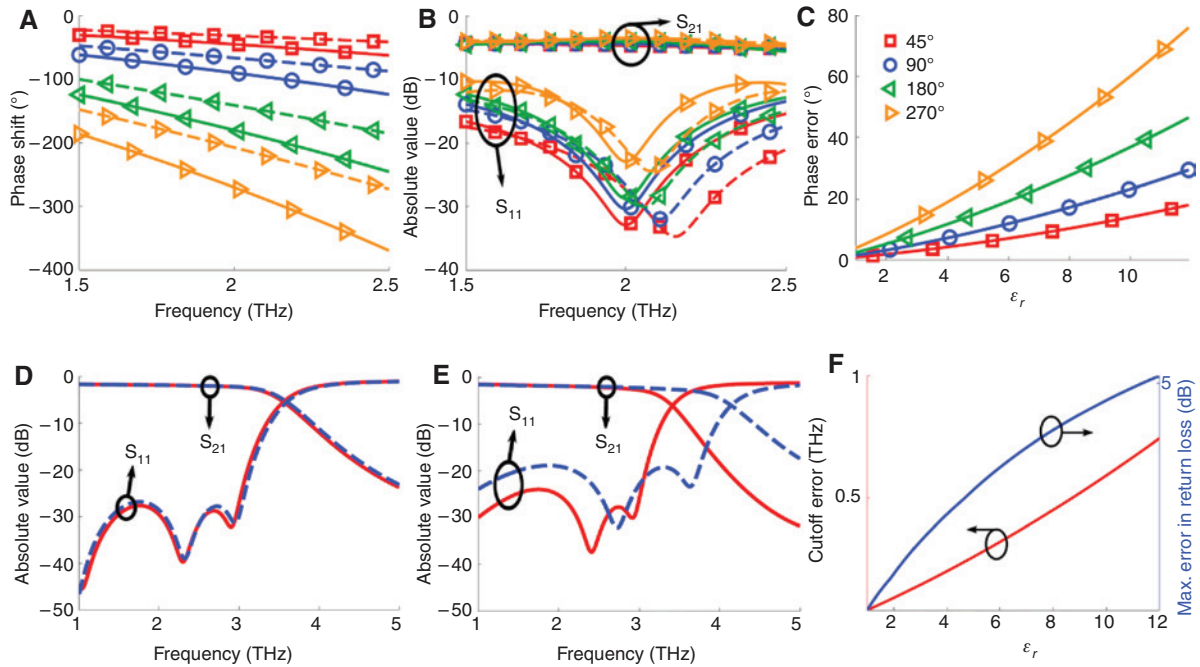
Figure 9: Influence of spatial dispersion in the response of graphene-based digital load-line phase shifters (top row) and low-pass filters (bottom row) [54] implemented by double-gated graphene parallel-plate waveguides.
The analysis of the phase shifter includes (A) phase difference between ports, (B) scattering parameters, and (C) phase error due to spatial dispersion versus the permittivity of the surrounding media. The 7th-degree low-pass filter is designed and analyzed in (D) free space and (E) embedded in Si ($\varepsilon_r \approx 11.0$). The error in the cutoff frequency and maximum in-band reflection due to graphene nonlocality as a function of surrounding permittivity is shown in panel (F). Solid line: results neglecting spatial dispersion effects; dashed line: results including spatial dispersion effects. Further details of the devices can be found in [54].

cylindrical configuration, as shown in Figure 10A and B. These configurations [47, 50, 52] realize electrically small THz antennas with tunable properties, providing large tunability of the resonant frequency, while keeping constant a very high antenna input impedance. Very importantly, such large values permit very good matching with photomixers and other embedded optical sources that

usually present very high input impedances, thus boosting the overall antenna radiation efficiency, as can be seen in Figure 10C. These resonant configurations are very promising to enhance the response of future THz communication and sensing systems.

In order to further control the direction of the radiated beam, a graphene-based THz leaky-wave antenna
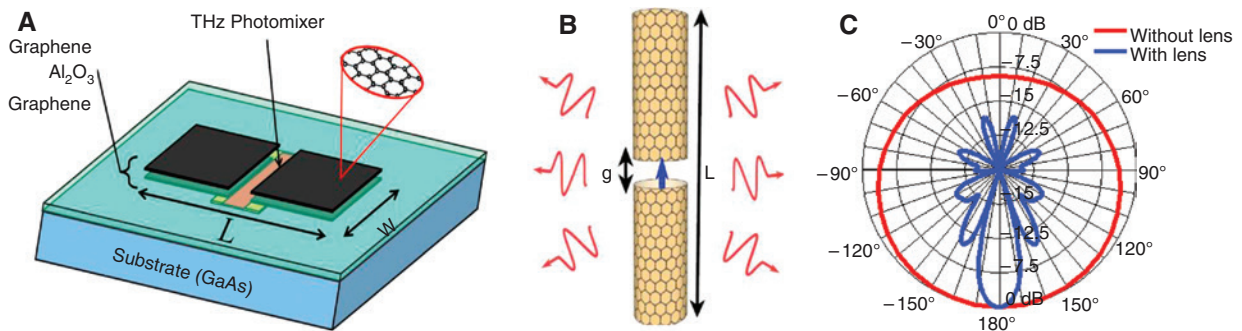

Figure 10: Graphene-based reconfigurable resonant antennas excited by a photomixer or a plasmonic optical source at its gap (from [47, 50, 52]).
(A) Planar structure composed of two graphene self-biasing patches. (B) Graphene cylindrical waveguide. (C) H-plane radiation diagram of the planar antenna at 1.8 THz.

for electronic beamscanning was recently proposed [102], as shown in Figure 11A. This THz antenna consists of a graphene monolayer with a set of polysilicon pads located beneath it. Thanks to the gate-tuned conductivity of graphene, the use of multiple cascaded gates may electronically modulate the surface reactance. In the zero bias condition, the graphene monolayer provides a "slow-wave" propagating SPP mode. When the gate electrodes are properly biased, a "digitized" sinusoidal modulation may be applied to the surface reactance of graphene, introducing high-order spatial harmonics that can support a "fast-wave" leaky mode. By varying the modulation periods through different bias setups, the THz beam can be steered over a wide range of scan angles. Another promising structure [51] consists of a width-modulated graphene strip able to couple ultraconfined surface plasmons to free-space propagating waves, while providing customized coupling angle, radiation rate, and exotic beam steering functionalities by simply applying a unique and modest DC bias to the antenna's ground plane. It is also important to mention that even more advanced designs able to implement nonreciprocal responses can be achieved by exploiting the spatiotemporal modulation of graphene [55], allowing to dramatically modify the radiation pattern of antennas when operating in transmission or reception mode and to,

under time-reversal, transmit and receive SPPs oscillating at different frequencies. However, in order to digitize the required sinusoidal surface reactance and reduce the radiation side-lobes, it is necessary to use a large number of gate electrodes underneath the graphene, which increases the fabrication complexity. An alternative solution able to solve such technological challenges is shown in Figure 11B, which employs the exotic acousto-optic effect of graphene.

It is well known that periodic corrugations on metallic surfaces can generate SPP resonances for various frequencies and angles of arrival of the exciting electromagnetic field. Similar ideas have been applied to excitations of propagating SPPs on a graphene sheet [103, 104]. In order to efficiently couple the incident photon into the propagating SPP mode, metallic gratings with suitable periods are typically required for matching their momentum, ensuring that the incident plane wave from free space can be coupled into the slow surface wave on the graphene sheet. Recently, an acousto-optical approach has been proposed to efficiently couple the incident radiation into propagating SPP mode on the graphene surface. Due to the large Young modulus and extreme thinness of graphene, it is possible to model elastic vibrations of graphene in the transverse direction with the scalar biharmonic equation: $(\Delta^2 - \beta_b^4 + \kappa / D)W = q$, where W, q, β_b, κ, and D represent
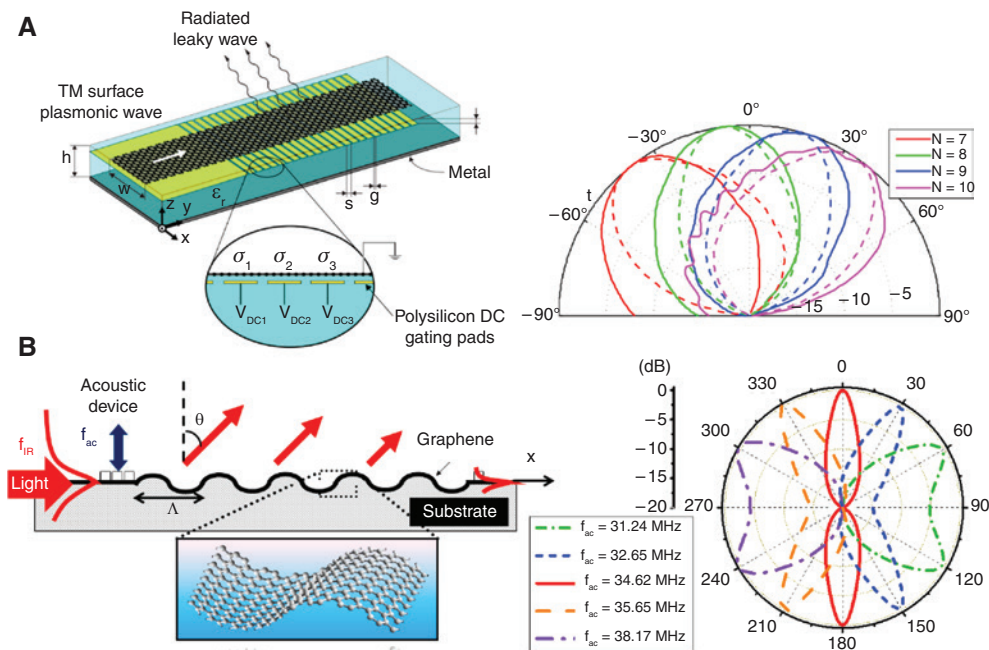
Figure 11: (A) Graphene-based leaky-wave antenna for electronic beam scanning. By electronically varying the number of bias pads per period (*N*), the THz beam (2 THz) can be scanned in free space. (B) Graphene-based analog leaky-wave antenna for acoustic-based beam scanning, with the angle of radiation as a function of acoustic frequency. Both devices show reconfigurable beamsteering effect at a locked frequency.

the vertical displacement field, source of vibration, flexural wave number, stiffness of the substrate, and the flexural rigidity, respectively [103]. The flexural wave traveling on a graphene surface that satisfies the biharmonic equation can be accurately modeled as the acoustic phonon modes with static grating of period $\Lambda_b = 2\pi / \mathrm{Re}[\tilde{\beta}_b]$ [103]. The periodic nano-corrugations introduced by elastic vibrations can excite the spatial (Floquet) harmonics, necessary for coupling the infrared incident waves from free space into the propagating SPP modes in graphene. Based on the electromagnetic reciprocity, the acousto-optical effect may realize reconfigurable THz and infrared leaky-wave antennas, which exploit the continuous, sinusoidal diffraction grating on graphene surface to transform the propagating surface wave into a leaky wave, with desired angles of departure, as shown in Figure 11B [105]. Moreover, since the period and depth of nanogratings are controlled by the acoustic frequency, it is possible to steer a directive beam into the far field at a constant infrared frequency, which is very different from conventional leaky-wave antennas that operate based on sweeping the electromagnetic frequency. Since the guided SPP mode excited in graphene is typically a slow wave with complex wave number $\mathrm{Re}[\beta_{\mathrm{SPP}}] \gg k_0$, the leaky (radiation) modes require the excitation of negative spatial harmonics, yielding a beam angle as a function of acoustic frequency ω_{ac} and electromagnetic waves ω, as well as the Fermi energy of graphene E_F:

$$\theta_0 = \sin^{-1}\left(\frac{\mathrm{Re}[\beta_{\mathrm{SPP}}(\omega, E_F)]}{k_0} - N\frac{\lambda_0}{\Lambda_{bh}(\omega_{ac})}\right). \qquad (14)$$

For the dominant TM plasmonic mode, β_{SPP} can be obtained from the dispersion relation in Eq. (8). It is common to take $N = -1$ spatial harmonic to avoid the undesired grating lobes in the backfire direction. The normalized radiation patterns calculated using a modified array factor method [105] are presented in Figure 11B (right panel), showing that a graphene leaky-wave antenna, with $E_F = 0.5$ eV, can steer the beam from backfire to endfire at a fixed MIR frequency $\omega/(2\pi) = 30$ THz, by simply tuning the frequency of flexural wave produced by an acoustic synthesizer (e.g. surface acoustic wave devices), and the results are well predicted by Eq. (14). We note that the switching speed of this acousto-optical device can be quite fast (MHz and GHz modulation speed), which may be of interest for realizing high-speed beamforming and beamsteering antennas fed by guided surface waves.

The interband loss mechanism of graphene becomes dominant at NIR frequencies and surface plasmons cannot be formed and sustained at its surface [18], which is the case for all previously presented examples operating at low THz frequencies. However, it is interesting to note that the properties of graphene can still be electrically controlled [106] even at these high frequencies, due to the strong variation in its carrier density and, as a result, doping level. Therefore, it is expected that its tunable properties will lead to altered scattering or transmitting responses at NIR or even optical frequencies when graphene is ingeniously combined with plasmonic metasurface [107] or nanoantenna [108] structures. However, graphene can only interact with the tangential (in-plane) electric field components of the impinging electromagnetic radiation due to its one-atom thickness. The ultrathin nature of graphene in the out-of-plane direction leads to very weak interaction with the normal (out-of-plane) electric field components of the incident electromagnetic wave.

To this end, an alternative hybrid graphene/all-dielectric metasurface design is presented in Figure 12A to achieve tunable and modulated transmission at NIR frequencies [109]. The presented all-dielectric hybrid metasurface is composed of periodically arranged pairs of asymmetric silicon (Si) nanobars with graphene placed on top of this configuration. The dimensions of the metasurface are highly subwavelength compared with the wavelength NIR radiation. This dielectric metasurface can sustain trapped magnetic resonances with a sharp Fano-type transmission or reflection signature [110]. The strong in-plane electric field distribution at the resonance is computed and shown in the inset of Figure 12B. One-atom-thick CVD graphene can be transferred and placed over this dielectric metasurface using standard transfer techniques [111]. Very strong transmission modulation is obtained at NIR telecom wavelengths when the doping level of graphene is increased, as it can be seen in Figure 12B. The enhanced in-plane fields along the all-dielectric metasurface strongly interact with the tunable properties of graphene. This leads to strong coupling between the incoming electromagnetic radiation and graphene. The transmission amplitude modulation of the proposed structure is presented in a more quantitative way by calculating the difference in transmission between heavily doped ($E_F = 0.75$ eV) and undoped ($E_F = 0$ eV) graphene. The absolute value of the transmission difference $\Delta T' = |(E_F = 0.75 \text{ eV}) - T(E_F = 0 \text{ eV})|$ is plotted in Figure 12C as a function of the impinging's radiation wavelength. Interestingly, the transmission difference ΔT (modulation) can reach values higher than 60% at the Fano resonance transmission dip ($\lambda = 1.59$ μm). Note that moderate modulation is also obtained within a narrow
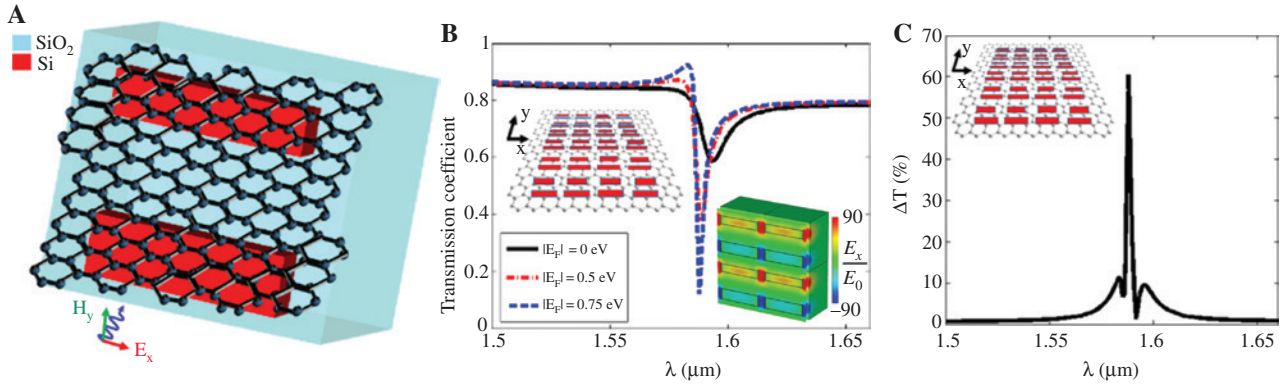
Figure 12: Hybrid graphene/dielectric metasurface configuration.
(A) Unit cell geometry of the proposed hybrid planar modulation device. (B) Strong transmission modulation for different doping levels of graphene. The field enhancement distribution is shown in the inset at the resonance. (C) Transmission difference between undoped and heavily doped graphene. More than 60% transmission modulation can be obtained in a narrow frequency region.

wavelength range around the resonance transmission dip. In this hybrid configuration, the in-plane resonant fields interact strongly with the in-plane graphene properties and strong electro-optical modulation is obtained at the transmission spectrum of this device. Several new integrated nanophotonic components are envisioned based on the proposed device, such as efficient ultrathin electro-optical transmission and reflection modulators and switches.

3 Nonlinear optical and active plasmonic prospects of graphene

Optical nonlinearities play a central role in the operation of a wide variety of integrated photonic devices, such as local light sources, electro-optical modulators, optical switches, and optical transistors. Studies of nonlinear optical properties of graphene represent a promising direction for optical experiments on the newly discovered Dirac materials with gapless, linear energy dispersion [112–116]. Due to the strong affinity of graphene for interacting with photons and its unique electronic properties, graphene becomes an exciting new candidate for providing nonlinear optical functionalities in nanoscale photonic devices. The unique linear energy dispersion of planar (e.g. graphene) and buckled (e.g. silicene and germanene) 2D Dirac materials endows them with nonlinear optical responses, which may even leverage the plasmonic resonances in the long-wavelength infrared region. At high enough field intensities, the dynamic conductivity of graphene becomes nonlinear, which can be analytically obtained from the kinetic Boltzmann equation [114]

or the semiconductor Block equation [115, 116], accounting for both the intraband and interband motions of electrons around the Dirac points. In this scenario, the time-dependent surface current density is in the form of a Fourier series $\mathbf{J}(t) = \sum_{m=0}^{m=+\infty} (1/2)(\mathbf{J}^{(m\omega)} e^{-im\omega t} + c.c)$, and, typically, only the first few terms actually contribute to graphene's electromagnetic response [117]. At long wavelengths, the important surface current components in graphene, when illuminated with monochromatic light of angular frequency ω, are the linear current $\mathbf{J}^{(1,\omega)}$ and the third-order nonlinear currents induced by the three-photon process $\mathbf{J}^{(3,\omega)}$ and $\mathbf{J}^{(3,3\omega)}$, where the former one, related with the nonlinear conductivity $\sigma^{(3)}(\omega; \omega, \omega, -\omega)$, is responsible for the self-action bistable effect and the later one, related with $\sigma^{(3)}(3\omega; \omega, \omega, \omega)$, is responsible for the third-harmonic generation. Typically, due to the inversion symmetry of the honeycomb lattice of graphene, the even-order nonlinearities are absent.

To date, the experimental demonstration of nonlinear optical properties of graphene flakes has been reported by several groups [113]. It has been shown that at NIR wavelengths, a graphene monolayer exhibits a remarkably high third-order optical nonlinearity, being independent of the wavelengths of incident light. It was shown that graphene produces strong third-order nonlinear optical response, described by nonlinear susceptibility $|\chi^{(3)}| \sim 10^{-7}$ esu (electrostatic units), which is comparable to that of other strongly nonlinear materials, such as carbon nanotubes [113]. However, in contrast to carbon nanotubes, this nonlinear response is rather dispersionless in the NIR to visible wavelength regions (emission with wavelength of 760–840 nm). The third-order nonlinearity of a material is described by the polarization $P^{(3)}(\omega_e) = \chi^{(3)} E(\omega_1) E(\omega_2) E(\omega_3)$, where ω_1, ω_2, and ω_3 are the frequencies of the electric field, E, of the incident laser.

In the degenerate four-wave mixing process shown in Figure 13A, where the two mixing frequencies are equal (e.g. $\omega_1 = \omega_3$), the frequency of emitted light is $\omega_e = 2\omega_1 - \omega_2$. Figure 13B shows the measured nonlinear signal from a monolayer flake as a function of the emission wavelength λ_e for several combinations of pump wavelengths λ_1 and λ_2. In all measurements, a clear spike in emission can be observed at the wavelength corresponding to the condition $\omega_e = 2\omega_1 - \omega_2$. By changing the pump wavelengths, one can investigate the dispersion of the nonlinear signal. It is evident from Figure 13B that the nonlinear signal wavelength is independent of the wavelength, as a result of the linear energy dispersion of graphene, where all photon energies in the four-wave mixing process can match electronic transitions, as shown in Figure 13B. The wavelength-independent, large third-order susceptibility of graphene ($|\chi^{(3)}| \sim 10^{-7}$ esu) is greater than that of most plasmonic material, such as gold, of the same thickness [113]. The strong nonlinear optical response of graphene may be utilized for imaging purposes, with image contrasts of graphene that are orders of magnitude higher than those obtained using linear microscopy.

THz amplification in photoexcited graphene was theoretically and experimentally studied earlier by Rana [17] and Ryzhii et al. [118–121] and recently detailed by Hamm et al. [122], who have considered the realistic collision loss and the effect of temperature and doping on the plasmon gain spectrum. Graphene's nonequilibrium THz properties are especially interesting, for which the population inversion and, thus, negative dynamic conductivity (THz gain) can take place in an optically pumped graphene monolayer, due to the cascaded optical-phonon emission and interband transitions around the Dirac point [118–121], as illustrated in Figure 14A. Under sufficiently strong optical excitation (e.g. photodoping by NIR and visible lasers), the interband emission of photons may prevail over the intraband Drude absorption, and thus, the real part of the dynamic conductivity of graphene can be made negative, particularly for pristine graphene at low temperatures. As a result, under the nonequilibrium condition, graphene could be seen as a distributed component with negative surface resistance, related to the THz gain. The photoexcited electron-hole pairs in graphene splits the Fermi level into two quasi-Fermi levels E_{Fn}, $E_{Fp} = \pm \varepsilon_F$ that, respectively, define the electron and hole concentrations. Since the relaxation time for intraband transitions is of the order of $\tau \approx$ ps, which is faster than the recombination time $\tau \approx$ ns for electron-hole pairs [123], the population inversion can be achieved with the optical pumping. Under sufficiently strong optical excitation, the interband emission of photons may prevail over the intraband Drude absorption, and therefore, the real part of the dynamic conductivity of graphene Re[σ] can be negative. Due to the unique gapless energy spectra of electrons and holes in graphene, the negative Re[σ] can occur at relatively low frequencies, i.e. the THz spectral range. The nonequilibrium dynamic conductivity of graphene, as a function of quasi-Fermi levels determined by the pump intensity, can be modeled using Green's functions [118–121] that include interband and intraband contributions (σ_{inter} and σ_{intra}). Re[σ_{inter}] could be negative, which, however, must compete with the positive Re[σ_{intra}]. Due to the unique gapless energy spectra of electrons and holes in graphene, Re[σ] can occur at relatively low frequencies ($\hbar\omega < 2\varepsilon_F$) provided that
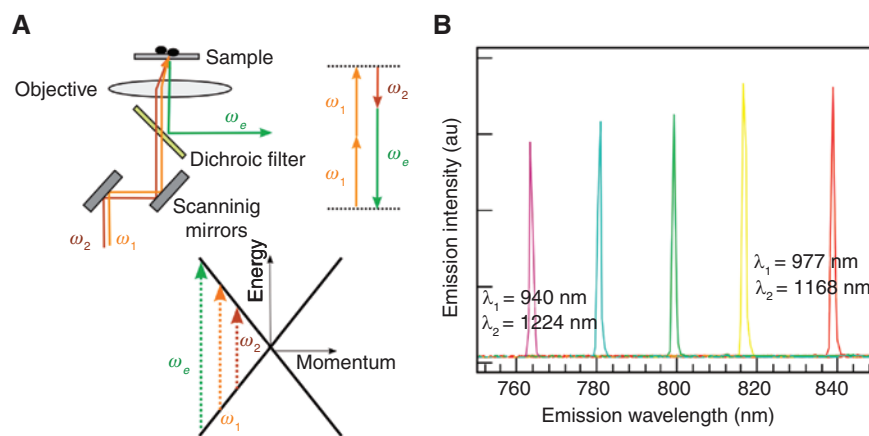
Figure 13: (A) Diagram of energy conservation in four-wave processes, which are based on the linear band structure of graphene with the three-photon energies (arrows) involved. Experimental layout, indicating the pump beams with frequencies ω_1, ω_2, and the emission beam with frequency ω_e. (B) Emission spectra of a graphene flake excited with pump light of different wavelengths (λ_1, λ_2): (940 nm, 1224 nm), (950 nm, 1210 nm), (958 nm, 1196 nm), (967 nm, 1183 nm), and (977 nm, 1168 nm) [113].
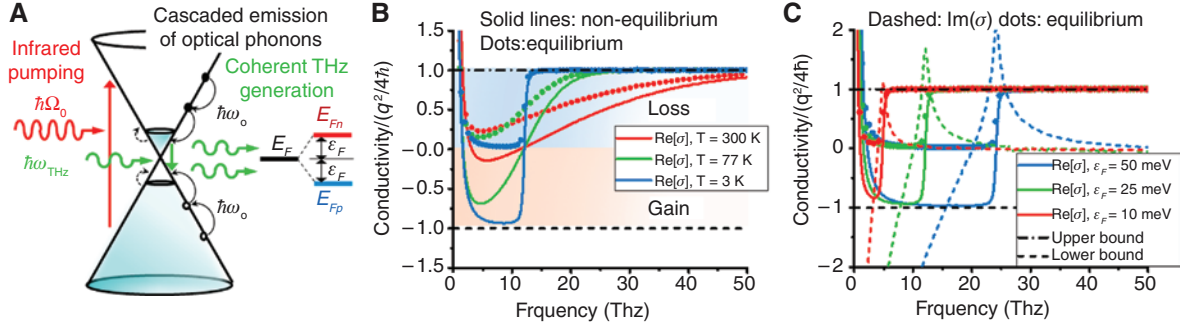
Figure 14: (A) Schematics of THz lasing in a pristine graphene ($E_F = 0$ eV) triggered by optical pumping. (B) Frequency dispersion of the real conductivity Re[σ] for a pristine graphene before (dots) and after (solid lines) the optical pumping, under different temperatures. (C) Frequency dispersion of real (solid lines) and imaginary (dashed lines) conductivity for a pristine graphene photoexcited to different quasi-Fermi energies at low temperatures ($T = 3$ K).

$$\mathrm{Re}[\sigma_{\mathrm{intra}}] = \frac{2q^2 k_B T \tau}{\pi \hbar^2 (1 + \omega^2 \tau^2)} \ln[1 + e^{\varepsilon_F / k_B T}] < |\mathrm{Re}[\sigma_{\mathrm{inter}}]|$$

$$\approx \left| \frac{q^2}{4\hbar} \tanh\left(\frac{\hbar\omega - 2\varepsilon_F}{4 K_B T} \right) \right|. \tag{15}$$

Figure 14B shows the real-part nonequilibrium conductivity Re[σ] of a graphene monolayer against the frequency, showing that negative conductivity and therefore THz gain may occur over a broad frequency range.

Combining these aspects with enhanced light-matter interactions of THz plasmons in graphene may open a plethora of applications, such as loss-compensated and lasing plasmonic devices [17]. Moreover, this active plasmonic material offers an ideal platform for studying THz parity-time (PT) symmetric systems, which exhibit exotic reciprocal and unidirectional scattering properties [124], technologically viable with spatially modulation of gain and loss. Therefore, the proposed PT symmetric THz devices may be feasible, particularly for singularity-enhanced sensing and probing applications. We note that some recent works have reported that for lossy graphene having a short phenomenological relaxation time (impurity-limited lifetime), the transient optical gain and population inversion in optically pumped graphene could last for only a short period of time ($\sim$ ps scale). However, there are many time-resolved THz microscopic techniques and applications that use a short-pulsed THz (picosecond/femtosecond) wave for the study of dynamics on extremely short time, instead of continuous waves. The measured time-domain signals can be processed by a Fourier transform to recover the frequency domain spectral information. Recently, there have been several experimental and theoretical works investigating the transient population inversion and THz plasmon gain in graphene and their possible gain effect in a time-domain analysis [120].

4 2D materials beyond graphene

In this section, we review the significant recent advances and important new developments in 2D materials "beyond graphene". The great success of graphene plasmonics has inspired research seeking for new 2D materials. One particular popular group of new 2D materials are transition-metal dichalcogenide monolayers, such as MoS_2, which act as 2D semiconductors and are promising candidates for the creation of future nanophotonic planar components. For example, plasmonic hot electron has been shown to enhance hydrogen evolution reaction [125] or to induce reversible 2H-1T phase transition on MoS2 monolayers [126]. However, MoS_2 suffers from intrinsically weak absorption ($\sim$ 3%) combined with low photoluminescence (PL) quantum yield (0.5%) [127]. These are general drawbacks, which apply to all 2D materials including graphene. To alleviate these problems, recently, researchers [128] have placed a MoS_2 monolayer in the nanogap of a plasmonic nanopatch antenna [129–131], as schematically shown in the inset of Figure 15. Based on this hybrid plasmonic/MoS_2 configuration, used in other contexts, such as in the interaction between graphene quantum dots [132] or gold nanoparticles [133] with MoS_2 layers, they were able to simultaneously enhance the absorption and quantum yield of MoS_2. The intrinsic excitonic PL emission of MoS_2 was enhanced by 56 times due to the placement of the plasmonic nanoantenna [128]. The obtained experimental results are shown in Figure 15. The control sample (MoS_2 on substrate/blue line in Figure 15) and nanoantenna (MoS_2 in nanogap/red line in Figure 15) are excited by the same excitation power. In addition, the shape of the PL spectrum is also modified by the addition of the nanoantenna. It becomes narrower and slightly ($\sim$ 5 nm) red-shifted (red line in the inset of Figure 15) relative to the intrinsic spectrum of the control sample (blue line in the
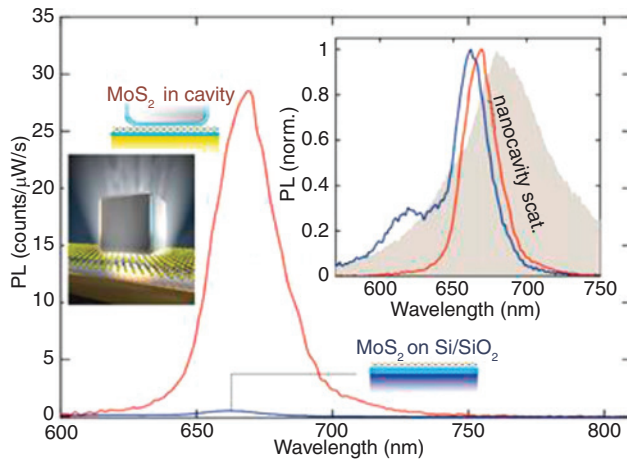
Figure 15: Hybrid nanoantennas with 2D materials (MoS$_2$). Enhanced PL of MoS$_2$ is obtained when it is combined with nano-patch antennas.

inset of Figure 15). Hence, plasmonic nanoantenna configurations can enhance and tune the absorption, PL, and other classical and quantum properties of MoS$_2$ or other 2D materials. In addition, arrays of nanoantennas forming metasurfaces are the ideal platforms to be hybridized with several 2D materials to obtain planar reconfigurable nanophotonic devices with new functionalities.

Another very promising 2D plasmonic material able to operate at near and mid infrared frequencies is black phosphorus (BP) [134–137] (see Figure 16). This material inherently exhibits an anisotropic conductivity, arising from a puckered crystalline structure that has lower symmetry compared with graphene (see Figure 16A), and a bandgap that covers a broad energy range, being increased monotonically from 0.3 eV to around 2 eV as the material thickness decreases from the bulk to a monolayer configuration.

Very importantly, BP supports the propagations of ultra-confined surface plasmons that can be easily manipulated – as well as the material's exotic band structure and electronic properties – by applying external mechanical strain or electrostatic/magnetostatic fields. Figure 16B shows a possible effective conductivity tensor of BP versus frequency, illustrating that when appropriately biased to have certain chemical potentials – defined here as the energy between the edge of the conduction band to the Fermi level – BP offers rich possibilities to inherently support exotic hyperbolic, anisotropic and σ-near-zero plasmons. In addition, Figure 16C reveals that BP also provides a large enhancement of the spontaneous emission rate of dipoles located nearby, which we attribute to the excitation and propagation of extremely anisotropic SPPs. It should be highlighted here that the finite velocity of electrons along BP may not be able to follow the locally predicted fast variations of the supported and extremely confined surface waves, so it is anticipated that nonlocal effects will play a key role in the development of future reconfigurable communication and sensing systems based on BP.

5 Conclusions

We have reviewed recent theoretical and experimental advances on graphene plasmonics and optoelectronics, as well as their practical applications in the THz-to-IR spectral range. We have first discussed the large body of recent works utilizing SPPs in graphene, associated with its Drude-type conductivity with a tunable plasma frequency ranging from THz to infrared. We have discussed how, by electrostatically/acoustically modulating or
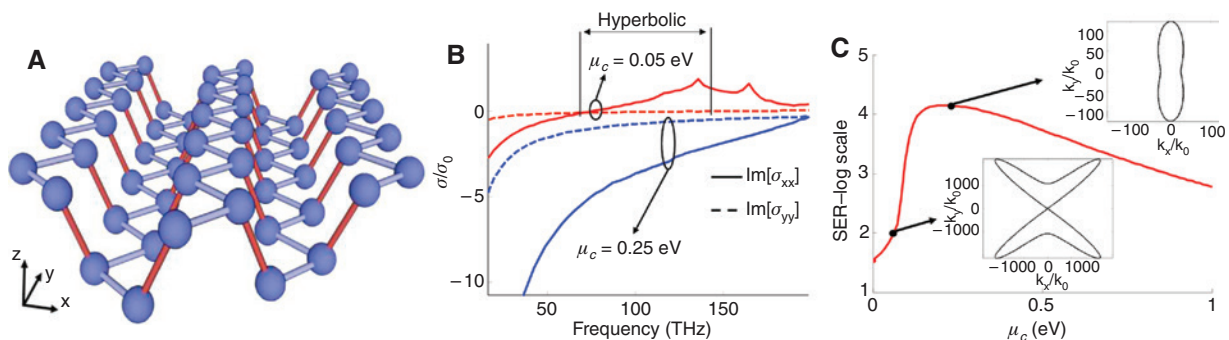
Figure 16: Electromagnetic response of BP (from [137]).
(A) Lattice structure of a monolayer BP sheet. Different colors are used for visual clarity. (B) Example of BP optical conductivity tensor for two different chemical potentials. (C) Spontaneous emission rate (in log scale) of a z-oriented emitter at 80 THz located 10 nm above a BP layer versus the material chemical potential. Insets show two different isofrequency contours of the supported plasmons.

lithographically patterning a graphene monolayer, one may be able to fully manipulate, enhance, and control the guided propagation, scattering, and radiation of long-wavelength light, similar to metal optics that deals with NIR and visible light. We have also presented the broadband and large nonlinear optical conductivity of graphene (orders of magnitude greater than plasmonic metals with similar thickness), uniquely existing in gapless 2D Dirac materials, which may provide interesting nonlinear optical responses, such as the multiple wave mixing related to the third-order susceptibility. We mentioned the possibility of achieving the THz plasmon gain in an optically pumped graphene, which may find potential applications in tunable THz laser and PT-symmetric systems. Finally, we highlight some viable 2D materials beyond graphene for flatland plasmonic and photonic platforms and their enabled device applications.

References

[1] Novoselov KS, Geim AK, Morozov SV, et al. Electric field effect in atomically thin carbon films. Science 2004;306:666–9.

[2] Geim AK, Novoselov KS. The rise of graphene. Nat Mater 2007;6:183–91.

[3] Neto AHC, Guinea F, Peres NMR, Novoselov KS, Geim AK. The electronic properties of graphene. Rev Mod Phys 2009;81:109–62.

[4] Meric I, Han MY, Young AF, Ozyilmaz B, Kim P, Shepard KL. Current saturation in zero-bandgap, top-gated graphene field-effect transistors. Nat Nanotechnol 2008;3:654–9.

[5] Lin YM, Dimitrakopoulos C, Jenkins KA, et al. 100-GHz transistors from wafer-scale epitaxial graphene. Science 2010;327:662.

[6] Wong HSP, Akinwande D. Carbon nanotube and graphene device physics. London, Cambridge University Press, 2009.

[7] Banszerus L, Schmitz M, Engels S, et al. Ballistic transport exceeding 28 μm in CVD grown graphene. Nano Lett 2016;16:1387–91.

[8] Yea J, Craciunc MF, Koshinod M, et al. Accessing the transport properties of graphene and its multilayers at high carrier density. Proc Natl Acad Sci 2011;108:13002–6.

[9] Stankovicha S, Dikina DA, Pinera RD, et al. Synthesis of graphene-based nanosheets via chemical reduction of exfoliated graphite oxide. Carbon 2007;45:1558–65.

[10] Li X, Cai W, An J, et al. Large-area synthesis of high-quality and uniform graphene films on copper foils. Science 2009;324:1312–4.

[11] Kim KS, Zhao Y, Jang H, et al. Large-scale pattern growth of graphene films for stretchable transparent electrodes. Nature 2009;457:706–10.

[12] Gusynin VP, Sharapov SG, Carbotte JP. Magneto-optical conductivity in graphene. J Phys Cond Matter 2007;19:026222.

[13] Hanson GW. Dyadic Green's functions and guided surface waves for a surface conductivity model of graphene. J Appl Phys 2006;103:064302.

[14] Hanson GW. Quasi-transverse electromagnetic modes supported by a graphene parallel-plate waveguide. J Appl Phys 2008;104:084314.

[15] Hanson GW. Dyadic Green's functions for an anisotropic, nonlocal model of biased graphene. IEEE Trans Antenna Propagat 2008;56:747–57.

[16] Falkovsky LA, Pershoguba SS. Optical far-infrared properties of a graphene monolayer and multilayer. Phys Rev B 2007;76:153410.

[17] Rana F. Graphene terahertz plasmon oscillators. IEEE Trans Nanotech 2008;7:91–9.

[18] Jablan M, Buljan H, Soljacic M. Plasmonics in graphene at infrared frequencies. Phys Rev B 2009;80:245435.

[19] Vakil A, Engheta N. Transformation optics using graphene. Science 2011;332:1291–4.

[20] Chen PY, Alù A. Atomically thin surface cloak using graphene monolayers. ACS Nano 2011;5:5855–63.

[21] Bao Q, Zhang H, Wang B, et al. Broadband graphene polarizer. Nat Photonics 2011;5:411–5.

[22] Koppens FHL, Chang DE, Garcia de Abajo FJ. Graphene plasmonics: a platform for strong light-matter interactions. Nano Lett 2011;11:3370–7.

[23] Fang Z, Thongrattanasiri S, Schlather A, et al. Gated tunability and hybridization of localized plasmons in nanostructured graphene. ACS Nano 2013;7:2388–95.

[24] Thongrattanasiri S, Koppens FHL, García de Abajo FJ. Complete optical absorption in periodically patterned graphene. Phys Rev Lett 2012;108:047401.

[25] Grigorenko AN, Polini M, Novoselov KS. Graphene plasmonics. Nat Photonics 2012;6:749–58.

[26] Pile D. Plasmonics: graphene shrinks light. Nat Photonics 2013;7:511.

[27] Chen J, Badioli M, Alonso-González P, et al. Optical nano-imaging of gate-tunable graphene plasmons. Nature 2012;487:77–81.

[28] Fei Z, Rodin AS, Andreev GO, et al. Gate-tuning of graphene plasmons revealed by infrared nano-imaging. Nature 2012;487:82–5.

[29] Maier SA. Plasmonics: fundamentals and applications. New York, Springer, 2007.

[30] Maier SA, Brongersma ML, Kik PG, Meltzer S, Requicha AAG, Atwater HA. Plasmonics – a route to nanoscale optical devices. 2001;13:1501–5.

[31] Zayats AV, Smolyaninov II, Maradudin AA. Nano-optics of surface plasmon polaritons. Phy Rep 2005;408:131–314.

[32] Ozbay E. Plasmonics: merging photonics and electronics at nanoscale dimensions. Science 2006;311:189–93.

[33] Dawlaty JM, Shivaraman S, Strait J, et al. Measurement of the optical absorption spectra of epitaxial graphene from terahertz to visible. Appl Phys Lett 2008;93:131905.

[34] Lee SH, Choi M, Kim TT, et al. Switching terahertz waves with gate-controlled active graphene metamaterials. Nat. Materials 2012;11:936–41.

[35] Chuang FT, Chen PY, Cheng TC, Chien CH, Li BJ. Improved field emission properties of thiolated multi-wall carbon nanotubes on a flexible carbon cloth substrate. Nanotechnology 2007;18:395702.

[36] Bao Y, Zu S, Zhang Y, Fang Z. Active control of graphene-based unidirectional surface plasmon launcher. ACS Photonics 2015;2:1135–40.

[37] Fang Z, Wang Y, Liu Z, et al. Plasmon-induced doping of graphene. ACS Nano 2012;6:10222–8.

[38] Huang H, Tao L, Liu F, et al. Chemical-sensitive graphene modulator with a memory effect for internet-of-things applications. Microsys Nanoeng 2016;2:16018.

[39] Ju L, Velasco J Jr., Huang E, et al. Photoinduced doping in heterostructures of graphene and boron nitride. Nat Nanotech 2014;9:348–52.

[40] Gómez-Díaz JS, Perruisseau-Carrier J. Graphene-based plasmonic switches at near infrared frequencies. Opt Exp 2013;32:15490–504.

[41] Yan H, Li X, Chandra B, et al. Tunable infrared plasmonic devices using graphene/insulator stacks. Nat Nanotech 2012;7:330–4.

[42] Bao Q, Loh KP. Graphene photonics, plasmonics, and broadband optoelectronic devices. ACS Nano 2012;6:3677–94.

[43] Gómez-Díaz JS, Tymchenko M, Alù A. Hyperbolic plasmons and topological transitions over uniaxial metasurface. Phys Rev Lett 2015;114:233901.

[44] Gómez-Díaz JS, Tymchenko M, Alù A. Hyperbolic metasurfaces: surface plasmons, light-matter interactions, and physical implementation using graphene strips. Optic Mater Express 2015;5:2313–29.

[45] Correas-Serrano D, Gómez-Díaz JS, Tymchenko M, Alù A. Nonlocal response of hyperbolic metasurfaces. Opt Express 2015;23:29434–338.

[46] Trushkov I, Iorsh I. Two-dimensional hyperbolic medium for electrons and photons based on the array of tunnel-coupled graphene nanoribbons. Phys Rev B 2015;92:045305.

[47] Tamagnone M, Gómez-Díaz JS, Mosig JR, Perruisseau-Carrier J. Analysis and design of terahertz antennas based on plasmonic resonant graphene sheets. J Appl Phys 2012;112:114915.

[48] Carrasco E, Perruisseau-Carrier J. Reflectarray antenna at terahertz using graphene. IEEE Antenna Wireless Propagat Lett 2013;12:253–6.

[49] Llatser I, Kremers C, Cabellos-Aparicio A, Jornet JM, Alarcon E, Chigrin DN. Graphene-based nano-patch antenna for terahertz radiation. Photon Nanostruct Fundam Appl published on-line, 2012.

[50] Tamagnone M, Gómez-Díaz JS, Mosig JR, Perruisseau-Carrier J. Reconfigurable THz plasmonic antenna concept usinga graphene stack. Appl Phys Lett 2012;101:214102.

[51] Gómez-Díaz JS, Esquius-Morote M, Perruisseau-Carrier J. Plane wave excitation-detection of non-resonant plasmons along finite-width graphene strips. Opt Express 2013;21:24856–72.

[52] Correas-Serrano D, Gómez-Díaz JS, Alù A, Alvarez-Melcon A. Electrically and magnetically biased graphene-based plasmonic cylindrical waveguides: analysis and application as reconfigurable antennas. IEEE Trans THz Sci Technol 2015;5:951–60.

[53] Chen PY, Argyropoulos C, Alù A. Terahertz antenna phase shifters using integrally-gated graphene transmission-lines. IEEE Trans Antennas Propagat 2013;61:1528–37.

[54] Correas-Serrano D, Gómez-Díaz JS, Alvarez-Melcon A. On the influence of spatial dispersion on the performance of graphene-based plasmonic devices. IEEE Antennas Wireless Propag Lett 2014;13:345–8.

[55] Correas-Serrano D, Gómez-Díaz JS, Sounas D, Alvarez-Melcon A, Alù A. Non-reciprocal graphene devices and antennas at THz based on spatio-temporal modulation. IEEE Antennas Wireless Propag Lett 2016;15:1529–33.

[56] Sensale-Rodriguez B, Yan R, Kelly MM, et al. Broadband graphene terahertz modulators enabled by intraband transitions. Nat Commun 2012;3:780. doi:10.1038/ncomms1787.

[57] Amin M, Farhat M, Bagci H. A dynamically reconfigurable Fano metamaterial through graphene tuning for switching and sensing applications. Sci Rep 2013;3:2105.

[58] Gómez-Díaz JS, Moldovan C, Capdevilla S, et al. Self-biased reconfigurable graphene stacks for terahertz plasmonics. Nat Commun 2015;6:6334.

[59] Chen PY, Alù A. A terahertz photomixer based on plasmonic nanoantennas coupled to a graphene emitter. Nanotechnology 2013;24:455202.

[60] Rzhii V, Ryzhii M, Mitin V, Shur MS, Satou A, Otsuji T. Terahertz photomixing using plasma resonances in double-graphene layer structures. J Appl Phys 2013;113:174506.

[61] Putz S, Gmitra M, Fabian J. Optical conductivity of hydrogenated graphene from first principles. Phys Rev B 2014;89:035437.

[62] Matthes L, Pulci O, Bechstedt F. Optical properties of two-dimensional honeycomb crystals graphene, silicene, germanene, and tinene from first principles. New J Phys 2014;16:105007.

[63] Hwang EH, Adam S, Das Sarma S. Carrier transport in two-dimensional graphene layers. Phys Rev Lett 2007;98:186806.

[64] Ju L, Geng B, Horng J, et al. Graphene plasmonics for tunable terahertz metamaterials. Nat Nanotech 2011;6:630–4.

[65] Yan H, Li Z, Li X, Zhu W, Avouris P, Xia F. Infrared spectroscopy of tunable Dirac terahertz magneto-plasmons in graphene. Nano Lett 2012;12:3766–71.

[66] Chen PY, Soric J, Alù A. Invisibility and cloaking based on scattering cancellation. Adv Mater 2012;24:281–304.

[67] Soric JC, Chen PY, Kerkhoff A, Rainwater D, Melin K, Alù A. Demonstration of an ultralow profile cloak for scattering suppression of a finite-length rod in free space. New J Phys 2013;15:033037.

[68] Alù A, Engheta N. Cloaking a sensor. Phys Rev Lett 2009;102:233901.

[69] Chen PY, Soric J, Padooru YR, Bernety HM, Yakovlev AB, Alù A. Nanostructured graphene metasurface for tunable terahertz cloaking. New J Phys 2013;15:123029.

[70] Hu JQ, Bando Y, Xu FF, et al. Growth and field-emission properties of crystalline, thin-walled carbon microtubes. Adv Mater 2004;16:153–6.

[71] Akyildiz IF, Jornet JM. The internet of nano-things. IEEE Wireless Communicat 2010;17:58–63.

[72] Jornet JM, Akyildiz IF. Graphene-based nano-antennas for electromagnetic nanocommunications in the terahertz band. Proceedings of 7th European Conference on. Antennas and Propagation (EuCAP). 2010;1–5.

[73] Abadal S, Alarcón E, Cabellos-Aparicio A, Lemme M, Nemirovsky M. Graphene-enabled wireless communication for massive multicore architectures. IEEE Commun Mag 2013;51:137–43.

[74] Farhat M, Rockstuhl C, Bağcı H. A 3D tunable and multi-frequency graphene plasmonic cloak. Opt Express 2013;21:12592–603.

[75] Christensen T, Jauho AP, Wubs M, Mortensen NA. Localized plasmons in graphene-coated nanospheres. Phys Rev B 2015;91:125414.

[76] Forouzmand A, Yakovlev AB. Electromagnetic cloaking of a finite conducting wedge with a nanostructured graphene meta-surface. IEEE Trans Antenna Propagat 2015;63:2191–202.

[77] Alaee R, Farhat M, Rockstuhl C, Lederer F. A perfect absorber made of a graphene micro-ribbon metamaterial. Opt Express 2012;20:28017–24.

[78] Chen PY, Farhat M, Bağcı H. Graphene metascreen for designing compact infrared absorbers with enhanced bandwidth. Nanotechnology 2015;26:164002.

[79] Zheludev N. The road ahead for metamaterials. Science 2010;328:582–3.

[80] Chen PY, Farhat M, Alù A. Bistable and self-tunable negative-index metamaterial at optical frequencies. Phys Rev Lett 2011;106:105503.

[81] Hadad Y, Steinberg BZ. Quasistatic resonance of a chemical potential interruption in a graphene layer and its polariz-ability: the mixed-polarity semilocalized plasmon. Phys Rev B 2013;88:075439.

[82] Tretyakov S. Analytical modeling in applied electromagnetics. London, Artech House Publishers, 2003.

[83] Fang Z, Wang Y, Schlather AE, et al. Active tunable absorp-tion enhancement with graphene nanodisk arrays. Nano Lett 2014;14:299–304.

[84] Chen PY, Alù A. Terahertz metamaterial devices based on graphene nanostructures. IEEE Trans THz Sci Technol 2013;3:748–56.

[85] Kern DJ, Werner DH, Lisovich M. Metaferrites: using electro-magnetic bandgap structures to synthesize metamaterial ferrites. IEEE Trans Antenna Propagat 2005;53:1382–9.

[86] Mosallaei H, Sarabandi K. Antenna miniaturization and band-width enhancement using a reactive impedance substrate. IEEE Trans Antenna Propagat 2004;52:2403–14.

[87] Luukkonen O, Simovski C, Granet G, et al. Simple and accurate analytical model of planar grids and high-impedance surfaces comprising metal strips or patches. IEEE Trans Antenna Propa-gat 2008;56:1624–32.

[88] Engheta N. Thin absorbers using space-filling-curve high-impedance surfaces. IEEE AP-S International Symposium. San Antonio, Texas, 2002.

[89] Liu X, Tyler T, Starr T, Starr AF, Jokerst NM, Padila WJ. Taming the blackbody with infrared metamaterials as selective thermal emitters. Phys Rev Lett 2011;107:045901.

[90] Correas-Serrano D, Gómez-Díaz JS, Tymchenko M, Alù A. Nonlocal response of hyperbolic metasurfaces. Opt Express 2015;23:29434–338.

[91] High AA, Devlin RC, Dibos A, et al. Visible-frequency hyperbolic metasurface. Nature 2015;522:192–6.

[92] Vakil A, Engheta N. Fourier optics on graphene. Phys Rev B 2012;85:075434.

[93] Skulason HS, Nguyen HV, Guermoune A, et al. 110 GHz measurement of large-area graphene integrated in low-loss microwave structures. Appl Phys Lett 2011;99:153504.

[94] Chen PY, Huang H, Akinwande D, Alù A. Graphene-based plas-monic platform for reconfigurable terahertz nanodevices. ACS Photonics 2014;1:647–54.

[95] Correas-Serrano D, Gómez-Díaz JS, Perruisseau-Carrier J, Alvarez-Melcon A. Graphene based plasmonic tunable low pass filters in the THz band. IEEE Transactions on Nanotech-nology 2014;13:1145–53.

[96] Lovat G, Hanson GW, Araneo R, Burghignoli P. Semiclassical spatially dispersive intraband conductivity tensor and quan-tum capacitance of graphene. Phys Rev B 2013;87:115429.

[97] Correas-Serrano D, Gómez-Díaz JS, Perruisseau-Carrier J, Alvarez-Melcon A. Spatially dispersive graphene single and parallel plate waveguides: analysis and circuit models. IEEE Trans Microw Theory Techniques 2013;61:4333–44.

[98] Lovat G, Burghignoli P, Araneo R. Low-frequency dominant-mode propagation in spatially dispersive graphene nanowave-guides. IEEE Trans Electromagn Compat 2013;11:1489–92.

[99] Falkovsky LA, Varlamov AA. Space-time dispersion of gra-phene conductivity. Eur Phys J B 2007;56:281–4.

[100] Filter R, Farhat M, Steglich M, Alaee R, Rockstuhl C, Lederer F. Tunable graphene antennas for selective enhancement of THz-emission. Opt Express 2013;21:3737–45.

[101] Fang Z, Liu Z, Wang Y, Ajayan PM, Nordlander P, Halas NJ. Graphene-antenna sandwich photodetector. Nano Lett 2012;12:3808–13.

[102] Esquius-Morote M, Gomez-Diaz JS, Perruisseau-Carrier J. Sinusoidally modulated graphene leaky-wave antenna for electronic beamscanning at THz. IEEE Trans Terahertz Sci Technol 2014;4:116–22.

[103] Farhat M, Guenneau S, Bagci H. Exciting graphene surface plasmon polaritons through light and sound interplay. Phys Rev Lett 2013;111:237404.

[104] Schiefele J, Pedros J, Sols F, Calle F, Guinea F. Coupling light into graphene plasmons through surface acoustic waves. Phys Rev Lett 2013;111:237405.

[105] Chen PY, Farhat M, Askarpour AN, Tymchenko M, Alù A. Infrared beam-steering using acoustically modulated surface plasmons over a graphene monolayer. J Opt 2014;16:094008.

[106] Wang F, Zhang Y, Tian C, et al. Gate-variable optical transitions in graphene. Science 2008;320:206–9.

[107] Emani NK, Chung TF, Kildishev AV, Shalaev VM, Chen YP, Boltasseva A. Electrical modulation of fano resonance in plasmonic nanostructures using graphene. Nano Lett 2014;14:78–82.

[108] Kim J, Son H, Cho DJ, et al. Electrical control of optical plas-mon resonance with graphene. Nano Lett 2012;12:5598–602.

[109] Argyropoulos C. Enhanced transmission modulation based on dielectric metasurfaces loaded with graphene. Opt Express 2015;23:23787–97.

[110] Zhang J, MacDonald KF, Zheludev NI. Near-infrared trapped mode magnetic resonance in an all-dielectric metamaterial. Opt Express 2013;21:26721–28.

[111] Suk JW, Kitt A, Magnuson CW, et al. Transfer of CVD-grown monolayer graphene onto arbitrary substrates. ACS Nano 2011;5:6916–24.

[112] Mikhailov SA, Ziegler K. Nonlinear electromagnetic response of graphene: frequency multiplication and the self-consistent-field effects. J Phys Condens Matter 2008;20:384204.

[113] Hendry E, Hale PJ, Moger J, Savchenko AK. Coherent nonlinear optical response of graphene. Phys Rev Lett 2010;105:097401.

[114] Peres NMR, Bludov YV, Santos JE, Jauho AP, Vasilevskiy MI. Optical bistability of graphene in the terahertz range. Phys Rev B 2014;90:125425.

[115] Mikhailov SA. Quantum theory of the third-order nonlinear electrodynamic effects of graphene. Phys Rev B 2016;93:085403.

[116] Cheng JL, Vermeulen N, Sipe JE. Third-order nonlinearity of graphene: effects of phenomenological relaxation and finite temperature. Phys Rev B 2015;91:235320.

[117] Boyd RW. Nonlinear Optics, 3rd ed. Cambridge, MA, USA, Academic Press, 2008.

[118] Ryzhii V, Ryzhii M, Otsuji T. Negative dynamic conductivity of graphene with optical pumping. J Appl Phys 2007;101:083114.

[119] Ryzhii V, Ryzhii M, Mitin V, Otsuji T. Toward the creation of terahertz graphene injection laser. J Appl Phys 2011;110:094503.

[120] Watanabe T, Fukushima T, Yabe Y, et al. Gain enhancement effect of surface plasmon polaritons on terahertz stimulated emission in optically pumped monolayer graphene. New J Phys 2013;15:075003.

[121] Popov VV, Polischuk OV, Nikitov SA, Ryzhii V, Otsji T, Shur MS. Amplification and lasing of terahertz radiation by plasmons in graphene with a planar distributed Bragg resonator. J Opt 2013;15:114009.

[122] Hamm JM, Page AF, Bravo-Abad J, Garcia-Vidal FJ, Hess O. Nonequilibrium plasmon emission drives ultrafast carrier relaxation dynamics in photoexcited graphene. Phys Rev B 2016;93:041408(R).

[123] Gierz I, Petersen JC, Mitrano M, et al. Snapshots of non-equilibrium Dirac carrier distributions in graphene. Nat Mater 2013;12:1119–24.

[124] Chen PY, Jung J. PT-symmetry and singularity-enhanced sensing based on photoexcited graphene metasurfaces. Phys Rev Appl 2016;5:064018.

[125] Kang Y, Gong Y, Hu Z, et al. Plasmonic hot electron enhanced MoS2 photocatalysis in hydrogen evolution. Nanoscale 2015;7:4482–8.

[126] Kang Y, Najmaei S, Liu Z, et al. Plasmonic hot electron induced structural phase transition in a MoS2 monolayer. Adv Mater 2014;26:6467–71.

[127] Mak KF, Lee C, Hone J, Shan J, Heinz TF. Atomically thin MoS2: a new direct-gap semiconductor. Phys Rev Lett 2010;105:136805.

[128] Akselrod GM, Ming T, Argyropoulos C, et al. Leveraging nanocavity harmonics for control of optical processes in 2D semiconductors. Nano Lett 2015;15:3578–84.

[129] Argyropoulos C, Ciracì C, Smith DR. Enhanced optical bistability with film-coupled plasmonic nanocubes. Appl Phys Lett 2014;104:063108.

[130] Akselrod GM, Argyropoulos C, Hoang TB, et al. Probing the mechanisms of large Purcell enhancement in plasmonic nano-antennas. Nature Photon 2014;8:835–40.

[131] Hoang TB, Akselrod GM, Argyropoulos C, Huang J, Smith DR, Mikkelsen MH. Ultrafast spontaneous emission source using plasmonic nanoantennas. Nat Commun 2015;6:7788.

[132] Li Z, Ye R, Feng R, et al. Graphene quantum dots doping of MoS2 monolayers. Adv Mater 2015;27:5235–40.

[133] Li Z, Xiao Y, Gong Y, et al. Active light control of the MoS2 monolayer exciton binding energy. ACS Nano 2015;9:10158–64.

[134] Low T, Roldán R, Wang H, et al. Plasmons and screening in monolayer and multilayer black phosphorus. Phys Rev Lett 2014;113:106802.

[135] Rodin AS, Carvalho A, Neto AC. Strain-induced gap modification in black phosphorus. Phys Rev Lett 2014;112:176801.

[136] Low T, Rodin AS, Carvalho A, et al. Tunable optical properties of multilayer black phosphorus thin films. Phys Rev B 2014;90:075434.

[137] Correas-Serrano D, Alvarez-Melcon A, Gomez-Diaz JS, Alù A. Strong light-matter interactions in thin black phosphorus films. IEEE International Symposium on Antennas and Propagation Symposium, Fajardo (Puerto Rico), 2016.